



# Instantaneous estimation and three-dimensional reconstruction of a highly modulated velocity field using finite-impulse-response-based spectral proper orthogonal decomposition

Ali Mohammadi<sup>1</sup> , Chris Morton<sup>2</sup>  and Robert J. Martinuzzi<sup>1</sup> 

<sup>1</sup>Department of Mechanical and Manufacturing Engineering, University of Calgary, 2500 University Drive NW, Calgary, AB T2N 1N4, Canada

<sup>2</sup>Department of Mechanical Engineering, McMaster University, 1280 Main Street West, Hamilton, ON L8S 4L7, Canada

**Corresponding author:** Robert J. Martinuzzi, [rmartinu@ucalgary.ca](mailto:rmartinu@ucalgary.ca)

(Received 27 March 2024; revised 15 October 2024; accepted 6 November 2024)

---

An adaptable estimation technique is presented to reconstruct time-evolving three dimensional (3-D) velocity fields from planar particle image velocimetry measurements. The methodology builds on the multi-time-delay estimation technique of Hosseini *et al.* (2015) by implementing the finite-impulse-response spectral proper orthogonal decomposition (FIR-SPOD) of Sieber *et al.* (2016). The candidate flow is the highly modulated turbulent near wake of a cantilevered square cylinder with a height-to-width ratio  $h/d = 4$ , protruding a thin laminar boundary layer ( $\delta/d = 0.21$  with  $\delta$  being the boundary layer thickness) at the Reynolds number  $Re = 10600$ , based on  $d$ . The novelty of the estimation technique is in using the modal space obtained by FIR-SPOD to better isolate the spatio-temporal scales for correlating velocity and pressure modes. Using FIR-SPOD, irregular coherent contributions at frequencies centred at  $f_{ac1} = (1 \pm 0.05)f_s$  and  $f_{ac2} = (1 \pm 0.1)f_s$  (with  $f_s$  the fundamental shedding frequency) could be separated, which was not possible using proper orthogonal decomposition. With the FIR-SPOD bases, the quality of the estimation improved significantly using only linear terms, and the correct phase relationships between pressure and velocity modes are retained, as is required for synchronizing coherent motions along the height of the obstacle. It is shown that a low-dimensional reconstruction of the flow field successfully captures the cycle-to-cycle variations of the dominant 3-D vortex shedding process, which give rise to vortex dislocation events. Thus, the present methodology shows promise in 3-D reconstruction of challenging turbulent flows, which exhibit non-periodic behaviour or contain multi-scale phenomena.

**Key words:** vortex shedding, vortex interaction, wakes

---

## 1. Introduction

In investigating the unsteady dynamics of turbulent flows, it is desirable to have access to three-dimensional (3-D) data. Such data enable analysis of the global dynamics of coherent motions, energy transfer between scales and processes underlying the Reynolds stress fields. While this information is directly available in computational studies, obtaining time-evolving 3-D rendering of the flow with simultaneously acceptable temporal and spatial resolutions remains challenging in experiments due to the limitations of current instrumentation. To address these limitations, sensor-based estimation methods have been used to synchronize uncorrelated planar particle image velocimetry (PIV) data. However, the quality of these estimations depends highly on (i) a suitable choice of sensor and (ii) the quality of the spatio-temporal separation of different motions through the implemented decomposition technique. In this study, we propose to use the finite-impulse-response spectral proper orthogonal decomposition (FIR-SPOD) of Sieber *et al.* (2016) to advance the multi-time-delay, pressure sensor-based estimation technique of Hosseini *et al.* (2015). The aim is to increase the accuracy of the estimations and phase synchronization of the different coherent motions, which is essential for dynamically consistent 3-D flow field reconstructions.

The 3-D flow reconstruction for flows expressing dominant periodic fluctuations are typically based on a phase-averaging technique (Hussain & Reynolds 1970). For wakes exhibiting Kármán-like vortex shedding, for example, velocity and a common reference signal, typically surface pressure, are conditionally averaged on the shedding phase. The reference signal phase is then used to synchronize the velocity measurements such as those obtained from uncorrelated PIV planes. Such reconstructions offer insights into the average or typical evolution of shed structures (Bourgeois *et al.* 2011; Kindree *et al.* 2018). Due to the averaging process, however, interactions with coherent motions at different scales are smeared out, such that processes underlying vortex deformations resulting in cycle-to-cycle variations are not captured.

Variants of stochastic estimation exploit the correlations between PIV and time-resolved surface pressure measurements to estimate the velocity field. Pressure sensors are often used because of the non-local nature of the pressure field, through the Poisson pressure equation, which favours remote sensing applications. Linear stochastic estimation (LSE) (Adrian 1979; Adrian & Moin 1988) is frequently linked to the proper orthogonal decomposition (POD) to estimate the POD temporal coefficients (modes) rather than the velocity field itself, as the modes set up an optimum basis to study the evolution of coherent motions (Taylor & Glauser 2004; Durgesh & Naughton 2010; Tu *et al.* 2013). As a variant of LSE, the extended POD, EPOD (Borée 2003), was proposed. The approach starts with POD of the signals from an array of surface pressure sensors. The temporal modal coefficients of the pressure are projected onto the velocity field, yielding extended (EPOD) velocity modes. While using all extended modes recovers LSE, it is observed that neglecting extended modes from poorly correlated pressure coefficients generally improves the estimation quality (Discetti *et al.* 2018).

Including the sensor signal time history has been shown to improve the estimation accuracy using LSE and EPOD. Durgesh & Naughton (2010) introduced the history of pressure sensors by adding virtual or time-delayed sensors. In this approach, referred to

as multi-time-delay estimation, for each physical sensor  $n$ , the sensor signal matrix is augmented by  $N_{vs}$  virtual sensors containing the time series of the  $n$ th sensor successively delayed by a constant  $\Delta\tau$ . Thus, the sensor matrix elements for the  $m$ th virtual sensor for the physical sensor  $n$ , located at  $\mathbf{X}_n$ , is represented as

$$p_{m+n+(n-1)N_{vs}}(t) = p(\mathbf{X}_n, t - m\Delta\tau) \quad (1.1)$$

with  $m=0$  corresponding to the physical sensor. The augmented sensor matrix is equivalent to the Henkel matrix common in control theory. For  $N_{ps}$  physical sensors and  $N_{vs}$  virtual (time-delayed) sensors for each physical one, the total number of sensors is  $M = N_{ps} \times (N_{vs} + 1)$ . As observed in the original study (Durgesh & Naughton 2010), the estimation quality depends on spacing between physical sensors,  $M$ ,  $\Delta\tau$  and an empirically determined optimal  $N_{vs}$ .

The implementation of multi-time delay with LSE and EPOD has been shown to improve estimations of weakly modulated quasi-periodic flows (Durgesh & Naughton 2010; Sicot *et al.* 2012; Hosseini *et al.* 2015). Discetti *et al.* (2018, 2019) suggested that eliminating poorly correlated data from the correlation matrix, using a normal distribution  $3\sigma$  criterion (with  $\sigma$  the standard deviation), removes the need for different time delays between modes in 3-D reconstruction. However, in their computational study of channel flow at a friction Reynolds number of  $Re_\tau = 1000$ , Discetti *et al.* (2018) emphasized the need to account for the convective speeds of different coherent motions. They also reported that velocity probes cannot effectively capture phenomena that do not convect downstream – an issue that presents significant challenges in studies involving generative adversarial networks (Cuéllar *et al.* 2024). The authors recommended placing probes at various spanwise locations, although this technique is intrusive in experimental studies and can significantly disrupt the flow. Additionally, not all instabilities are convective, necessitating the use of time-resolved pressure probes. These challenges highlight that the phase relationship between the sensor and different coherent motions cannot be captured with a single delay parameter using conventional decomposition techniques. In flows with multiple energetic motion scales, the estimation quality deteriorates rapidly when the sensor is positioned out of plane, which complicates the synchronization of global coherent motions in reconstructions from uncorrelated PIV planes.

Hosseini *et al.* (2015) addressed the issue of retaining the phase relationships between sensor and coherent motions by projecting the multi-time-delay surface pressure POD modes on the velocity POD modes to obtain orthogonal extended velocity modes. In contrast to using non-orthogonal representations, e.g. EPOD velocity modes, this approach enabled optimal delays to be calculated for individual pressure and velocity modes and a criterion for selecting  $N_{vs}$ . The method was shown to improve the estimation and synchronization of the dynamics for the five most energetic modes. They attributed the poorer performance for higher-order modes to an increasingly poorer separation of the scales of motion inherent to POD. This observation emphasizes the importance of selecting a decomposition technique yielding a suitable subspace for separating scales of motion.

More recently, machine learning and deep learning techniques have been widely applied in fluid dynamics (Duraismy *et al.* 2019). For instance, based on surface pressure of a cylinder, Manohar *et al.* (2022) trained artificial neural networks to predict velocity fields. Machine learning or deep learning techniques still require extracting the intrinsic physical features embedded in the data (Kutz 2017). For instance, in the study of Deng *et al.* (2019) who used long short-term memory neural networks, the dynamics of the estimated velocity field was poorly rendered for motions other than at the dominant frequency, and a physical interpretation of the resultant modal basis was challenging. Jin *et al.* (2020) considered the in-plane estimation of unsteady wake regions in the mid-span height plane of an infinite

cylinder for several flow regimes at Reynolds numbers of  $Re = 200, 500$  and  $24\,000$ . They proposed using the spatial functions of the most energetic POD modes and a bidirectional recurrent neural network for estimating the temporal coefficients from high-frequency velocity probe reference measurements. For the most energetic modes, associated with the Kármán vortex shedding frequency, a high estimation accuracy was reported over all  $Re$ . However, for higher-order modes, the estimation accuracy decreased substantially with increasing  $Re$ . This suggests that reliable estimations with machine learning tools still face challenges in retaining the footprints of coherent motions that do not convect downstream and also require implementation of decomposition techniques that can efficiently separate the spatio-temporal scales of coherent motions.

Exploiting resolvent analysis to estimate space–time flow statistics from a limited set of known data, as opposed to modelling spatial or temporal statistics independently (Towne *et al.* 2020; Martini *et al.* 2020; Amaral *et al.* 2021) has shown promise. This approach is based on using the known data to deduce the statistical characteristics of the nonlinear components that form a driving force in the linearized Navier–Stokes equations. By applying the resolvent operator, the unknown flow statistics are determined. For incompressible boundary layers and jets (Sasaki *et al.* 2017; Beneddine *et al.* 2017), the method is suggested to provide a viable means to perform real-time estimations without requiring the construction of reduced-order models (Martini *et al.* 2020). However, the quality deteriorates rapidly with distance from the sensor location. More importantly, the issue of synchronization of flow patterns (e.g. coherent motions) between different planar estimations for 3-D flow reconstructions has not been addressed with this method.

Other modal analysis techniques, such as discrete Fourier transform (DFT) or dynamic mode decomposition (DMD) have also been employed in flow estimation (Gomez *et al.* 2019; Chen *et al.* 2022). In DMD (Rowley *et al.* 2009; Schmid 2010), the focus is on spanning the mode space based on fixed frequencies to identify coherent structures. In turbulent flows, however, the coherent structures are naturally broadband phenomena and often contain inter-modal interactions. This makes a compact representation of coherent motions within the DMD mode space difficult. Furthermore, the resultant DMD modes are not orthogonal in the time domain, which raises challenges in flow reconstructions.

The FIR-SPOD (Sieber *et al.* 2016) technique bridges the gap between the energetically optimal POD (Sirovich 1987) mode space and spectrally resolved DFT or DMD. In this approach, a filter operation is applied to the correlation matrix in the form of a convolution. This allows the possible outcomes to maintain a balance between resolving turbulent spatio-temporal scales (as in DMD) and capturing significant portions of the turbulent kinetic energy (TKE) of the flow through a few modes (as in POD). Mohammadi *et al.* (2023) considered the cantilevered cylinder wakes and showed that, in comparison with traditional POD, FIR-SPOD better separates the modal energetic contributions within narrow spectral bandwidths with a small number of modes. For example, they could separate frequencies at  $(1 \pm 0.05)f_s$  and  $(1 \pm 0.1)f_s$  and associate them with modulations of the Kármán vortex shedding (at  $f_s$ ) due to a low-frequency motion, which was not possible using phase-averaging or traditional POD. This motivates the implementation of FIR-SPOD in the multi-time-delay estimation technique.

The candidate diagnostic flow considered in this study is the highly modulated near-wake region of a cantilevered square cylinder with a nominal height-to-width ratio ( $h/d$ ) of 4, protruding a laminar boundary layer with a relative thickness-to-height ratio ( $\delta/h$ ) of 0.21, at  $Re = U_\infty d/\nu = 10600$  (with  $U_\infty$  and  $\nu$  the free-stream velocity and kinematic viscosity, respectively). This flow has been subject of previous studies (Kindree *et al.* 2018; Mohammadi *et al.* 2022, 2023). Briefly, Kindree *et al.* (2018) identified mean dipole and descending vortices in the wake region, based on a phase-averaged reconstruction. The

dipole had previously been introduced as the footprint of vortical connector strands, which connect two successive Kármán vortices on opposite sides of obstacle's symmetry plane, ultimately forming half-loop shedding patterns (Bourgeois *et al.* 2011, 2013; Hosseini *et al.* 2013). The descending vortices capture the loci of initial connections between the connector strands and the forming Kármán vortex on the opposite sides (Mohammadi *et al.* 2022). These wakes are characterized by strong modulations, which are believed to result from interactions between different large-scale vortical structures. The motivation of this paper is to add to the understanding of these interactions by studying the deformation of the shed structures for different cycles of the shedding process.

This work advances velocity estimation techniques based on remote sensors, located outside of the velocity (PIV) measurement planes. It proposes FIR-SPOD as a suitable decomposition bases for separating the dynamics while retaining properties in the time domain, which permit low-dimensional representations through which contributions of coherent motions can be related to physical phenomena. The surface pressure is used to synchronize the uncorrelated PIV planes. Hence this work addresses synchronizing of the dynamics of different coherent motions in space. The technique is illustrated by using a 3-D reconstruction from uncorrelated PIV planes to investigate a highly modulated quasi-periodic wake.

The paper continues in five sections. Section 2 presents the experimental set-up, data acquisition process and analytical methodology, and § 3 provides some brief background on the physics of the candidate flow. Results are presented in the following two sections. Section 4 presents evaluations of the proposed estimation technique, whereas § 5 compares and discusses the flow physics during a typical and an interrupted shedding cycle. Section 6 provides conclusive remarks.

## 2. Data processing and estimation approach

In this section, first the key details of the experimental set-up for PIV and pressure sensor measurements are provided for completeness. Further details can be found in Kindree *et al.* (2018). Then, the analytical background on the decomposition of the flow field and pressure sensor-based estimation of the velocity field is presented.

### 2.1. Experimental set-up

The flow around an  $h/d \approx 4$  square cylinder ( $h = 51.1$  and  $d = 13.1$  mm) protruding a thin laminar boundary layer is experimentally investigated. Measurements were conducted in an open-test-section suction wind tunnel.

The velocity fields were acquired using stereoscopic PIV synchronized with surface pressure measurements. Figure 1 shows schematics of the test model, nomenclature, coordinate system and location of the PIV planes and pressure taps. The obstacle was mounted on a machined-flat rigid steel ground plate (the wall) of length, width and thickness 2500, 600 and 17.5 mm, respectively. The plate leading edge was a 4:1 (half) ellipse, with the minor axis matching the plate thickness. The intersection of the cylinder central axis with the plate marked the origin of the Cartesian coordinate system:  $x$ ,  $y$  and  $z$  are streamwise, lateral and spanwise directions, respectively. The corresponding velocity components are  $u$ ,  $v$ ,  $w$  for the instantaneous,  $U$ ,  $V$ ,  $W$  the mean and  $u'$ ,  $v'$ ,  $w'$  the fluctuating components. All coordinate variables and velocity components are non-dimensionalized by  $d$  and  $U_\infty$ , respectively.

The location of the pressure taps was determined based on earlier studies and preliminary PIV measurements. It has been determined that off-setting the pressure taps (1–6) on the obstacle sides generally resulted in a better discrimination of the

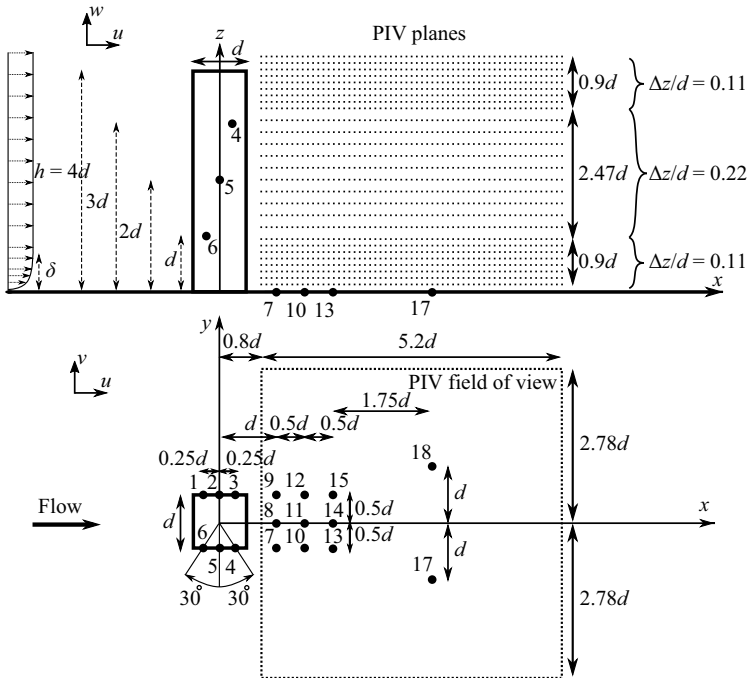


Figure 1. Schematics of the experimental set-up in the test section of the wind tunnel with the coordinate system and related nomenclature. Here,  $\bullet$  indicates the location of pressure sensors. The figure is reprinted from Kindree *et al.* (2018) with permission.

pressure fluctuation phases. When using either POD or FIR-SPOD, a stronger correlation between temporal coefficients of the pressure and velocity modes is observed. On the plate, the pressure taps are concentrated in the obstacle base region, where generally the magnitude of the spatial modal functions are largest. Taps 17 and 18 are located downstream of the mean recirculation region. The associated sensor data contributed to a better synchronization of the estimated modes related to the shed Kármán vortices.

The velocity fields were acquired using a LaVision FlowMaster PIV system on 27 horizontal planes, spanning  $0.8 \leq x \leq 6$  and  $-2.7 \leq y \leq 2.7$ , with a spacing of 0.11 mm for  $z < 0.9$  and  $3.37 < z \leq 4.27$  and 0.22 mm for  $0.9 \leq z \leq 3.37$ . Laskin nozzles, placed at the tunnel inlet, were used to generate olive oil particles (with a number-mean diameter of  $d_0 \approx 1 \mu\text{m}$ ).

The laser sheet was generated with a single cavity 20 mJ Photonics Industries 527 nm Nd-YLF laser, operated in twin-pulse mode. The laser sheet was approximately 2 mm thick using a cylindrical spherical lens combination (focal lengths: 800 and  $-20$  mm). Two FastCam SA4 CMOS cameras ( $1024 \times 1024$  pixels) were positioned symmetrically at  $\pm 30^\circ$  about  $y = 0$ . The pulse separation between images of a pair was  $30 \mu\text{s}$ . The PIV images were processed using LaVision's Davis 8.3 software. Interrogation windows of  $32 \times 32$  pixels with 50% overlap were used with a straddled arrangement. Where necessary, interrogation windows with a more refined resolution of  $16 \times 16$  pixels were used without overlap, which resulted in a spatial resolution of approximately  $0.09d$ . Image pairs were captured at a rate of  $f_{PIV} = 1200$  Hz, which is at least 10 points per shedding cycle. Six independent trials of 2700 snapshots were acquired for each plane. In general, four trials were sufficient for statistical convergence of the first and second statistical moments as well as the POD/SPOD modes (see Appendix B in Mohammadi *et al.* (2023)). The

maximum uncertainty of the free-stream mean and instantaneous velocity vectors were estimated (Wieneke 2015) to be  $\Delta U/U_\infty = \pm 0.027$  and  $\Delta u/U_\infty = \pm 0.053$ .

Surface pressure measurements and PIV planes were synchronized with a transistor-transistor-logic signal from the laser. All Sensors Corporation 5-INCH-D1-4V-MINI differential pressure transducers acquired pressure data from  $N_{ps} = 17$  pressure taps (with a 0.3 mm diameter), located on the obstacle faces and ground plate. The high-pressure side of the transducer was connected to the pressure taps and the low-pressure side was connected to the static port of the wind tunnel's Pitot-static tube via a manifold. A National Instrument NI 9 234 24-bit data acquisition interface was used to sample the pressure signals at 10.24 kHz. The signals were digitally filtered at 1 kHz using an eighth-order Butterworth filter applied forwards and backwards to correct for the filter-induced phase lag. The tapping-tubing-transducer system had a flat frequency response up to  $\approx 250$  Hz and the sensor resolution was  $\pm 1.3$  Pa. Calibration details can be found in Kindree *et al.* (2018).

Experiments were run at a nominal free-stream velocity  $U_\infty = 14.3$  m/s corresponding to  $Re \approx 10600$ . The nominal shedding frequency was  $St = f_s d/U_\infty = 0.11$ , such that  $f_s \approx 120$  Hz and  $f_{PIV} \approx 10f_s$ . The free-stream turbulence was less than 0.1%. The boundary layer developed naturally from the leading edge and was shown to follow the Balsius profile (Kindree *et al.* 2018). At the location of the obstacle with the obstacle removed (i.e.  $x = 0$  corresponds to a distance of 213 mm from the leading edge), the boundary layer thickness was measured to be  $\delta/h = 0.053$  ( $\delta/d = 0.21$ ), which is considered as thin (Sakamoto & Arie 1983; Sakamoto & Oiwake 1984). With  $\delta^*$ ,  $\theta$  and  $H = \delta^*/\theta$  being the displacement thickness, momentum thickness and shape factor,  $\delta^*/\delta = 0.35$ ,  $\theta/\delta = 0.13$  and  $H = 2.6$ .

## 2.2. Decomposition of flow fields

The velocity field,  $\mathbf{u}(\mathbf{x}, t)$ , is subject to a triple decomposition into a mean,  $\mathbf{U}(\mathbf{x})$ , coherent ( $\mathbf{u}_c(\mathbf{x}, t)$ ) and incoherent contributions ( $\mathbf{u}''(\mathbf{x}, t)$ ) (Hussain 1983)

$$\mathbf{u}(\mathbf{x}, t) = \mathbf{U}(\mathbf{x}) + \underbrace{\mathbf{u}_c(\mathbf{x}, t) + \mathbf{u}''(\mathbf{x}, t)}_{\mathbf{u}'(\mathbf{x}, t)}, \quad (2.1)$$

with  $\mathbf{u}'$  the total fluctuations. Bold symbols indicate vectors and the arguments  $\mathbf{x}$  and  $t$  represent location and time, respectively. Wherever clear, these arguments are implied for brevity.

For the velocity field, the snapshot POD (Sirovich 1987)/SPOD (Sieber *et al.* 2016) is used to determine  $\mathbf{u}_c$ . For the pressure field, the classical counterparts of these methods are used. For completeness, a brief overview of these methods is given below. Details of the mode selection are discussed in § 3.

### 2.2.1. Snapshot POD/SPOD

The snapshot POD/SPOD is more efficient for handling the PIV data, where the number of spatial points is higher than the number of snapshots. The POD reconstruction of the velocity field is defined as

$$\mathbf{u}'(\mathbf{x}, t) = \sum_{i=1}^N a^i(t) \boldsymbol{\phi}^i(\mathbf{x}), \quad (2.2)$$

where  $a^i$  and  $\phi^i$  are the temporal and spatial modal functions, respectively. Here,  $N$  is the total number of modes, which in the snapshot POD is equivalent to the total number of snapshots.

The correlation matrix  $\mathbf{R}$  is based on the inner product  $\langle \cdot, \cdot \rangle$  of two snapshots,  $\mathbf{u}'(\mathbf{x}, t_i)$  and  $\mathbf{u}'(\mathbf{x}, t_j)$

$$R_{i,j} = \frac{1}{N} \langle \mathbf{u}'(\mathbf{x}, t_i), \mathbf{u}'(\mathbf{x}, t_j) \rangle = \frac{1}{N} \int_A \mathbf{u}'(\mathbf{x}, t_i) \mathbf{u}'(\mathbf{x}, t_j) \, dx dy, \quad (2.3)$$

where  $A$  specifies the PIV domain. As  $\mathbf{R}$  is an  $N \times N$  real symmetric positive-definite matrix, its eigenvectors,  $a^i$ , are real and orthogonal to each other

$$\frac{1}{N} (a^i, a^j) = \lambda^i \delta_{ij}. \quad (2.4)$$

The  $\lambda_i$  are the eigenvalues of  $\mathbf{R}$  and show fluctuation energy of the corresponding  $a^i$ .  $(\cdot, \cdot)$  represents the scalar product. The modes are sorted by  $\lambda^i$  in a descending order. The sum of all  $\lambda^i$  is twice the total kinetic energy of the fluctuations over the domain  $A$

$$\text{TKE} = \frac{1}{2} \sum_{i=1}^N \lambda^i. \quad (2.5)$$

Finally,  $\phi^i$  are obtained by projecting  $\mathbf{u}'$  onto  $a^i$

$$\phi^i(\mathbf{x}) = \frac{1}{N\lambda^i} \sum_{j=1}^N a^i(t_j) \mathbf{u}'(\mathbf{x}, t_j). \quad (2.6)$$

The POD spatial modes are orthonormal by construction:  $\langle \phi^i, \phi^j \rangle = \delta_{ij}$ .

In the FIR-SPOD (Sieber *et al.* 2016), a low-pass filter is applied along the diagonals of  $\mathbf{R}$ . The elements of the resulting correlation matrix,  $\mathbf{S}$ , are given by

$$S_{i,j} = \sum_{k=-N_f}^{N_f} g_k R_{i+k,j+k}, \quad (2.7)$$

where  $g_k$  is the discrete representation of a Gaussian filter, with bandwidth  $(2N_f + 1)/f_{PIV}$

$$g_k = \frac{1}{\sqrt{2\pi} N_f} e^{-\frac{1}{2} \left(\frac{k}{N_f}\right)^2}. \quad (2.8)$$

The remainder of the procedure of snapshot SPOD is the same as for snapshot POD. The temporal modal coefficients remain orthogonal, but the spatial modes are no longer orthogonal (see Appendix A). The TKE is still represented as in (2.5) and if all modes are used for reconstruction, the flow field is fully recovered.

### 2.2.2. Classical POD/SPOD

The classical POD/SPOD approach is computationally more efficient for handling pressure data, which typically consist of long time series at a few locations. More precisely, the classical approach is more efficient if (i)  $M < N_s$  for POD and (ii)  $M \times (2N_f + 1) < N_s$  for the FIR-SPOD ( $M$ ,  $N_s$  and  $N_f$  are the total number of pressure sensors, total number of snapshots and SPOD filter parameter, respectively).

The POD of the pressure field,  $p$ , can be presented as

$$p(x_i, t) = P(x_i) + \sum_{n=1}^N b^n(t) \Psi^n(x_i), \quad (2.9)$$

where  $P$  is the mean pressure, and  $b^n$  are the temporal coefficients corresponding to spatial functions  $\Psi^n$ . In classical POD, the correlation matrix  $\mathbf{R}$  is a matrix (Sieber *et al.* 2016)

$$R_{i,j} = \frac{1}{N} \langle p'(x_i, t), p'(x_j, t) \rangle, \quad (2.10)$$

where  $p' = p - P$  is the fluctuating pressure. Here, the eigenvectors of  $\mathbf{R}$  form the spatial functions  $\Psi$  and temporal modes are obtained by projecting  $p'$  on  $\Psi$ .

The implementation of the filter operation in the classical FIR-SPOD is more delicate. The multi-time-shift correlation tensor,  $S_{i,j,k,l}$ , is formed

$$S_{i,j,k,l} = \frac{\sqrt{g_k g_l}}{MN \Delta t} \int p'(x_i, t - k \Delta t) p'(x_j, t - l \Delta t) dt, \quad (2.11)$$

with  $i, j = 1, \dots, M$  and  $k, l = -N_f, \dots, N_f$ . Here,  $g_k$  and  $g_l$  are the Gaussian filter coefficients. Note that in numerical implementation,  $S_{i,j,k,l}$  is reshaped into a matrix format:  $\tilde{S}_{(i+kM), (j+lM)}$ . The correlation tensor is now decomposed, such that

$$\sum_{l=-N_f}^{N_f} \sum_{j=1}^M S_{i,j,k,l} \tilde{\Psi}^n(x_j, \tau_l) = \mu^n \tilde{\Psi}^n(x_i, \tau_k), \quad (2.12)$$

where  $\tau_k = k \Delta t$ . The discrete convolution filter,  $\tilde{\Psi}^n$ , can be interpreted as a data-driven filter bank which allows for decomposition of time series into temporal coefficients

$$b^n(t) = \sum_{l=-N_f}^{N_f} \sum_{i=1}^M \sqrt{\frac{g_k}{M}} \tilde{\Psi}^n(x_i, \tau_k) p'(x_i, t - \tau_k). \quad (2.13)$$

Note that, while  $\tilde{\Psi}^n$ , which forms an orthonormal basis, is used to calculate the temporal coefficients, the spatial modes that are used to reconstruct and recover the original signal are the central part of  $\tilde{\Psi}^n$  (i.e.,  $\Psi^n = \tilde{\Psi}^n(x_i, 0)$ ), which in general, are not orthogonal.

Prior to either snapshot or classical POD/SPOD, a symmetric/antisymmetric split is carried out on the dataset to accelerate the convergence in terms of PIV snapshots needed (Holmes *et al.* 2012)

$$\begin{aligned} u_a(x, y, z, t) &= [u'(x, y, z) - u'(x, -y, z)]/2 \\ u_s(x, y, z, t) &= [u'(x, y, z) + u'(x, -y, z)]/2 \\ v_a(x, y, z, t) &= [v'(x, y, z) + v'(x, -y, z)]/2 \\ v_s(x, y, z, t) &= [v'(x, y, z) - v'(x, -y, z)]/2 \\ w_a(x, y, z, t) &= [w'(x, y, z) - w'(x, -y, z)]/2 \\ w_s(x, y, z, t) &= [w'(x, y, z) + w'(x, -y, z)]/2, \end{aligned} \quad (2.14)$$

where the spatial modes of the resulting symmetric and antisymmetric fields are orthogonal to each other by construction. For convenience, in the remainder of the text, temporal modes of both velocity and pressure modes associated with the antisymmetric field will be shown by  $a^n$  and symmetric ones with  $s^n$ , where  $n$  is the mode number. The velocity temporal modes will be accompanied by the subscript  $u$  (e.g.  $a_u^n$  and  $s_u^n$ ) and pressure temporal modes by the subscript  $p$  (e.g.  $a_p^n$  and  $s_p^n$ ).

### 2.3. Sensor-based flow estimation

In selection of the optimal number of virtual sensors ( $N_{vs}$ ) for periodic flows, first, the maximum time delay,  $\tau = N_{vs} \Delta\tau$ , needs to be identified (with  $\Delta\tau$  the time delay between two virtual sensors). Durgesh & Naughton (2010) and Sicot *et al.* (2012) showed empirically that an optimal value exists for  $\tau$ . Hosseini *et al.* (2015) recommended an optimal value for  $\tau$  to be close to the shedding period,  $1/f_s$ . According to Noack *et al.* (2005), at least four points per cycle are needed to resolve modes with strong harmonic contributions. Hosseini *et al.* (2015) suggested considering additional points to account for the cycle-to-cycle variations. Hence, to recover the second harmonics ( $2f_s$ ), at least 10 points per shedding cycle need to be considered (i.e.  $\Delta\tau = 1/10f_s$  and  $N_{vs} = 10$ ).

The velocity field is estimated from the pressure modes, obtained from  $M = N_{ps} \times (N_{vs} + 1) = 17 \times (10 + 1) = 187$  sensors (i.e. the velocity field estimation and reconstruction use all physical pressure sensors indicated in figure 1 and their corresponding virtual sensors)

$$\hat{\mathbf{u}}(\mathbf{x}, t_{est}) = \sum_{k=1}^{N_u} \hat{a}_u^k(t_{est}) \phi_u^k(\mathbf{x}), \quad (2.15)$$

$$\hat{a}_u^k(t_{est}) = \sum_{n=1}^{N_{mode}} a_p^n(t_{est}) \frac{\langle a_p^n(t) a_u^k(t) \rangle}{\lambda_p^n}, \quad (2.16)$$

where  $N_u$  represents the number of velocity modes used for estimating the velocity field  $\hat{\mathbf{u}}$ ,  $N_{mode}$  the number of pressure modes used for estimating each velocity coefficient  $\hat{a}_u^k$  and  $\langle . . \rangle$  the correlation function. Here,  $a_u^k$  and  $\phi_u^k$  are the velocity temporal and spatial POD/SPOD modes at each plane, respectively;  $a_p^n(t)$  are obtained from projecting  $p'$ , obtained concurrently with the velocity measurements, on the pressure spatial modes (using (2.13)). To ensure convergence of these spatial modes, they are obtained from performing POD/SPOD on all available trials (i.e.  $27 \times 6 = 162$  trials). The values  $a_p^n(t_{est})$  can be from any of the 27 sets of pressure POD/SPOD bases. For consistency in a 3-D reconstruction,  $a_p^n(t_{est})$  from the same trial is used to estimate the velocity field in all planes.

Equation (2.16) is in the form of Hosseini *et al.* (2015), where by the EPOD approach of Borée (2003) is recast in terms of the orthonormal velocity modes and the orthogonality condition is enforced. This form is consistent with the proposed linear modal relationship between pressure and velocity fluctuations described in Noack *et al.* (2005) and Noack (2006), who observed that this form is suitable for laminar and transitional unconditional unstable cylinder wakes and shear layers and more relevant in this study, for inhomogeneous turbulent wakes in general. In preliminary testing, the influence of quadratic terms in the pressure–velocity relationship was considered. It was found that these correlation coefficients were very small compared with the linear terms and below experimental uncertainty. These observations are consistent with earlier studies and thus these quadratic terms were not retained.

In the implementation of (2.16), modes for which the  $\langle a_p^n a_u^n \rangle$  are below the measurement uncertainty were not retained, following the practice of Discetti *et al.* (2018). As observed in Hosseini *et al.* (2015) and discussed by Discetti *et al.* (2018), retaining poorly correlated terms generally results in less accurate estimations. To account for time lags between the velocity and pressure fields, which can arise as a result of physical separation of the two fields or convective delays, the optimal time lag is found from the peak of the cross-correlation ( $r$ ) for all velocity and pressure mode combinations. Then, the correct phase

of estimated signal is recovered from delaying the pressure signal. For instance, assuming that only the correlation of  $s_u^\Delta$  and  $s_p^\Delta$  is non-vanishing in estimation of  $\hat{s}_u^\Delta$ , the optimal time lag ( $\tau_s^\Delta$ ) is found from  $r_{s_u^\Delta s_p^\Delta}(\tau) = (s_u^\Delta(t), s_p^\Delta(t + \tau)) / \sqrt{\lambda_{s_u^\Delta} \lambda_{s_p^\Delta}}$ . Thus

$$\hat{s}_u^\Delta(t_{est}) = s_p^\Delta(t_{est} - \tau_s^\Delta) \frac{\langle s_p^\Delta(t - \tau_s^\Delta) s_u^\Delta(t) \rangle}{\lambda_{s_p^\Delta}}. \tag{2.17}$$

### 3. Flow characteristics

The flow over a cantilevered square cross-section cylinder has been characterized in previous studies (Kindree *et al.* 2018; Mohammadi *et al.* 2023). It is dominated by quasi-periodic vortex shedding. Three energetically dominant frequencies exist in the near-wake region:  $f_s$  and  $2f_s$  corresponding to the first and second harmonics of Kármán vortex shedding, respectively, and  $f_L = 0.1f_s$ , corresponding to a low-frequency signature, associated with the flapping of the shear layers originating from the free end of the obstacle. Weaker peaks in the spectrum of the velocity fluctuations, at  $f_{ac1} = (1 \pm 0.05)f_s$  and  $f_{ac2} = (1 \pm 0.1)f_s$ , were also reported. These frequencies were attributed to the interactions between the Kármán vortex shedding and low-frequency signature from the free end (Mohammadi *et al.* 2023) and will be referred to as the accompanying frequencies.

Figure 2 illustrates the  $u$  and  $v$  spatial functions of selected POD (columns 1 and 2) and SPOD (columns 4 and 5) modes at  $z = 1.83$  (close to the mid-span height of the cylinder). This plane is chosen as it contains coherent motions associated with most of the aforementioned frequencies. To the right of each set, the power spectral density function (PSDF) of the respective coefficients of each mode is shown. Note that with mode pairs (i.e. with spectral energy concentration at the same frequency), only the first mode is shown for brevity.

For POD, the orthonormal mode basis for the velocity field is determined following the procedure of Hosseini *et al.* (2015). Here, only modes which show correlations with the pressure field above the uncertainty threshold are considered. Briefly:

- (i) From the antisymmetric field,  $\mathbf{u}_a$ , the two most energetic modes (i.e.  $\{\phi_a^1, \phi_a^2\}$ ) show dominant spectral peaks at  $f_s$  and are taken to represent the fundamental Kármán vortex shedding. Note that  $\{..,\}$  indicates two modes that constitute a mode pair.
- (ii) The symmetric component,  $\mathbf{u}_s$ , is further decomposed into (1) slow- and (2) fast-varying parts ( $\langle \mathbf{u} \rangle_G$  and  $\mathbf{u}_s^H$ , respectively). Here,  $\langle \mathbf{u} \rangle_G$  is calculated by applying a Gaussian filter on  $\mathbf{u}_s$

$$\langle \mathbf{u} \rangle_G(t) = \int_{-\infty}^{\infty} \mathbf{u}_s(\tau) g(t - \tau) d\tau. \tag{3.1}$$

The bandwidth of the Gaussian filter is set to be  $\sigma = 0.003$ . Hosseini *et al.* (2015) observed that applying a filtering operation accelerates the convergence of the low-frequency spatial modes as the slow-varying part has a time scale comparable to the PIV acquisition window. The first POD mode of  $\langle \mathbf{u} \rangle_G$  shows a strong spectral peak at  $f_L$  and is taken to represent the slow-varying signature (i.e.  $\phi_s^\Delta$ ). Thus,  $a_s^\Delta = (\mathbf{u}_s, \phi_s^\Delta)$ . Now,  $\mathbf{u}_s^H$  is obtained as

$$\mathbf{u}_s^H = \mathbf{u}_s - (\mathbf{u}_s, \phi_s^\Delta) \phi_s^\Delta. \tag{3.2}$$

The two most energetic  $\mathbf{u}_s^H$  POD modes (i.e.  $\{\phi_s^1, \phi_s^2\}$ ) show dominant spectral peaks at  $2f_s$  and represent the second harmonics of the Kármán vortex shedding.

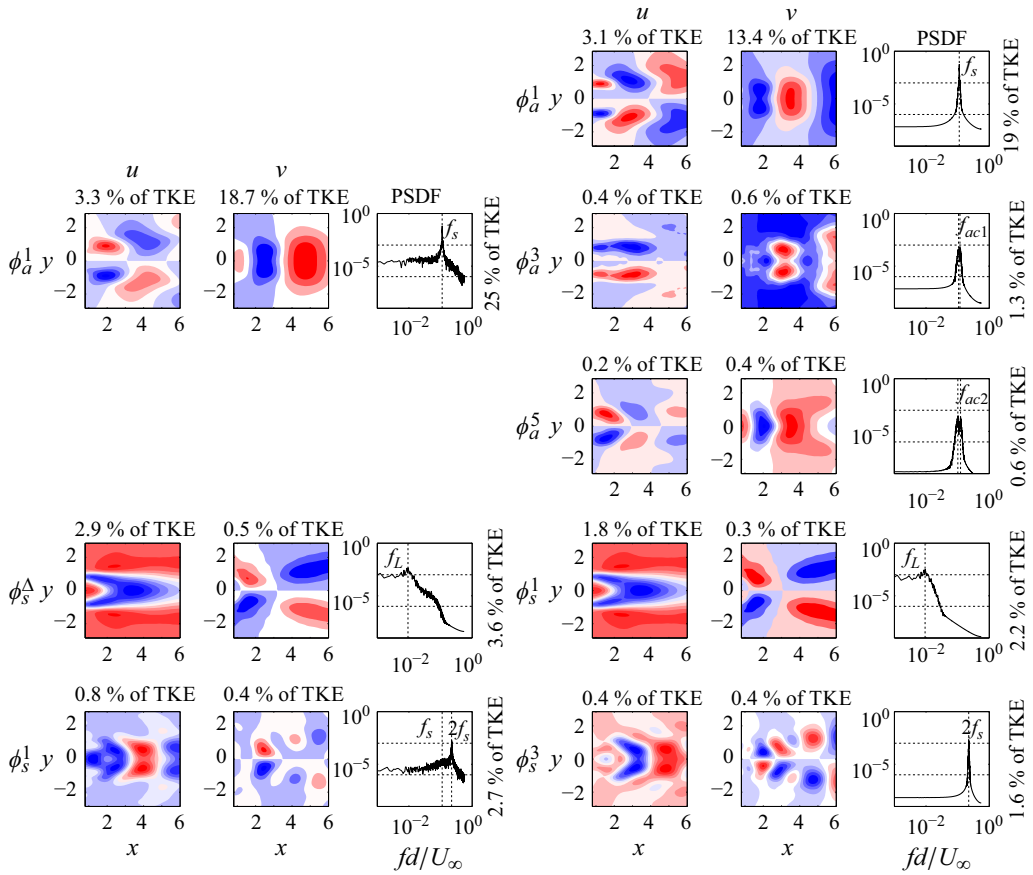


Figure 2. Decomposition of the velocity field at  $z = 1.83$ . Spatial modal functions for  $u$  and  $v$ , and PSDF from POD (left three columns) and SPOD ( $N_f = 64$ ; filter length of  $127/f_{PIV}$ ) (right three columns). For POD:  $\phi_a^1$ ,  $\phi_s^\Delta$ , and  $\phi_s^1$  represent the most energetic antisymmetric, slow-varying symmetric, and fast-varying symmetric modes, respectively. For SPOD:  $\phi_a^1$ ,  $\phi_a^3$  and  $\phi_a^5$  are the first modes of the first three most energetic antisymmetric mode pairs, respectively, and  $\phi_s^1$  and  $\phi_s^3$  are the first modes of the first two most energetic symmetric mode pairs, respectively.

The outlined procedure accelerates the spatial mode convergence, but does not affect the spectral characteristics of the temporal coefficients. The separation of frequencies is not ideal with the POD modes (third column in figure 2). For instance, the accompanying frequencies at  $f_{ac1}$  and  $f_{ac2}$  in the spectra of  $a_u^1$  are mixed with motions at  $f_s$ . Moreover, in the spectra of  $s_u^1$ , which is associated with motions at  $2f_s$ , energetic contributions exist around  $f_s$ .

For SPOD, it was verified that the spectral separation of modes makes the pre-filtering step (as described above for the POD case) unnecessary. However,  $N_f$  must be chosen carefully. Here,  $N_f$  is set to be 64 corresponding to a filter length of  $127/f_{PIV}$  ( $\approx 12.7/f_s$ ). Obtaining a finer resolution and separation of spectral dynamics with higher SPOD filter length comes at the penalty of representing less TKE. Thus, a balance needs to be maintained. Readers are referred to Appendix C of Mohammadi *et al.* (2023) for a more complete discussion on the selection of the filter parameter  $N_f$ .

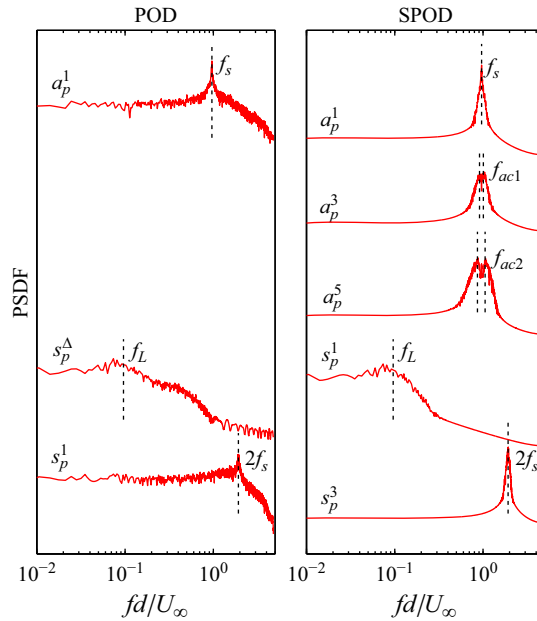


Figure 3. The PSDF of the temporal functions of the most energetic pressure POD/SPOD modes. For POD,  $a_p^1$ ,  $s_p^\Delta$  and  $s_p^1$  show dominant spectral behaviour around  $f_s$ ,  $f_L$  and  $2f_s$ , respectively. For SPOD,  $a_p^1$ ,  $a_p^3$ ,  $a_p^5$ ,  $s_p^1$  and  $s_p^3$  show dominant spectral behaviour around  $f_s$ ,  $f_{ac1}$ ,  $f_{ac2}$ ,  $f_L$  and  $2f_s$ , respectively. Spectra are offset for clarity.

In figure 2,  $\{\phi_a^1, \phi_a^2\}$  and  $\{\phi_s^3, \phi_s^4\}$  mode pairs correspond to the fundamental and second harmonics of Kármán vortex shedding at  $f_s$  and  $2f_s$ , respectively;  $\{\phi_s^1, \phi_s^2\}$  corresponds to a slow-varying mode with a low-frequency signature at  $f_L$ ; and  $\{\phi_a^3, \phi_a^4\}$  and  $\{\phi_a^5, \phi_a^6\}$  correspond to inter-harmonics at  $f_{ac1}$  and  $f_{ac2}$ , respectively. The motions at  $f_L$ ,  $f_s$ ,  $f_{ac1}$ ,  $f_{ac2}$  and  $2f_s$  appear in separate modes.

Figure 3 shows the PSDF of the temporal coefficients of the most energetic pressure POD/SPOD modes. These modes are obtained from performing classical POD and SPOD ( $N_f = 64$ ) on all 162 trials of available pressure data. Similar to the velocity field, for POD,  $a_p^1$ ,  $s_p^\Delta$  and  $s_p^1$  show spectral energy concentrations around  $f_s$ ,  $f_L$  and  $2f_s$ , respectively. Contributions at  $f_{ac1}$  and  $f_{ac2}$  are mixed with the spectra of  $a_p^1$  and  $a_p^2$  and cannot be separated. For SPOD, on the other hand,  $a_p^1$ ,  $a_p^3$ ,  $a_p^5$ ,  $s_p^1$  and  $s_p^3$  show important spectral energy contributions around  $f_s$ ,  $f_{ac1}$ ,  $f_{ac2}$ ,  $f_L$  and  $2f_s$ , respectively. This separation of dominant frequencies in both velocity and pressure SPOD modes suggests a potential in improving the quality of the correlation-based estimation procedure of Hosseini *et al.* (2015).

#### 4. Results – evaluation of the proposed technique

In this section, a comparative evaluation of the POD- and SPOD-based estimation is presented. In § 4.1, the actual and estimated modes at  $z = 1.83$  are compared by analysing temporal coefficients, residual values and reconstructed velocity fields. For all estimations in § 4.1, the reference pressure modes are naturally synchronized with the corresponding velocity modes (measured at the same time as the PIV measurements at  $z = 1.83$ ). In § 4.2,

POD	$a_u^1$	$a_u^2$	$s_u^\Delta$	$s_u^1$	$s_u^2$
$a_p^1$	2.43	<b>23.61</b>	0.02	0.15	0.37
$a_p^2$	<b>25.61</b>	2.20	0.01	0.23	0.28
$s_p^\Delta$	0.22	0.06	<b>3.71</b>	0.37	0.12
$s_p^1$	0.06	0	0	<b>2.43</b>	1.38
$s_p^2$	0.04	0.05	0	1.38	<b>2.19</b>

Table 1. Covariance magnitudes between selected velocity and pressure POD modes at  $z = 1.83$ . Mode pairs (mode) identified with the same frequency in both fields are separated with sidelines. The highest covariance magnitudes between each velocity mode and all pressure modes is bolded. Magnitudes less than 0.005 are replaced by 0.

SPOD	$a_u^1$	$a_u^2$	$a_u^3$	$a_u^4$	$a_u^5$	$a_u^6$	$s_u^1$	$s_u^2$	$s_u^3$	$s_u^4$
$a_p^1$	2.40	<b>22.46</b>	0.40	0.35	0.02	0.06	0	0	0	0
$a_p^2$	<b>22.45</b>	2.40	0.35	0.39	0.06	0.02	0	0	0	0
$a_p^3$	0.42	0.02	<b>1.18</b>	0.49	0.02	0	0	0	0	0
$a_p^4$	0.02	0.43	0.49	<b>1.18</b>	0	0.02	0	0	0	0
$a_p^5$	0.14	0.02	0.02	0.13	<b>0.52</b>	0.29	0	0	0	0
$a_p^6$	0.03	0.14	0.13	0.02	0.29	<b>0.52</b>	0	0	0	0
$s_p^1$	0	0	0	0	0	0	<b>2.62</b>	0.97	0	0
$s_p^2$	0	0	0	0	0	0	0.99	<b>1.97</b>	0	0
$s_p^3$	0	0	0	0	0	0	0	0	<b>1.63</b>	1.39
$s_p^4$	0	0	0	0	0	0	0	0	1.39	<b>1.63</b>

Table 2. Covariance magnitudes between selected velocity and pressure SPOD modes at  $z = 1.83$ . Mode pairs identified with the same frequency in both fields are separated with sidelines. The highest covariance magnitudes between each velocity mode and all pressure modes is bolded. Magnitudes less than 0.005 are replaced by 0.

the discussion is extended by estimating and analysing the temporal coefficients at other heights using common reference modes acquired from pressure data concurrently obtained with PIV measurements at  $z = 0.92$ .

#### 4.1. Estimation results using synchronized pressure data

In applying (2.16) and (2.17), it was mentioned that identifying the non-vanishing correlations and setting the remaining to zero improves the estimation. Here, this statement is considered more closely. Tables 1 and 2 present the covariance magnitudes between selected velocity and pressure POD/SPOD modes at  $z = 1.83$ , respectively. Mode pairs associated with the same dominant frequency(ies) in both fields are separated using sidelines (e.g.  $\{a_u^1, a_u^2\}$  and  $\{a_p^1, a_p^2\}$  are associated with  $f_s$ ).

In table 1, the covariance magnitudes are highest between modes in the same mode subspace. The covariance of higher-ranked pressure and velocity POD modes were negligible. Furthermore, it was verified that in performing the estimation, contributions due to correlations between the selected antisymmetric and symmetric modes or between

the slow-varying and fast-varying symmetric modes were negligible. This is consistent with the findings of Hosseini *et al.* (2015). Therefore, for estimation of the first two antisymmetric modes ( $\hat{a}_u^k$ ;  $k = 1$  and  $2$ ), only correlations with  $a_p^1$  and  $a_p^2$  are considered

$$\hat{a}_u^k(t_{est}) = \sum_{n=1}^2 a_p^n(t_{est} - \tau_a^n) \frac{\langle a_p^n(t - \tau_a^n) a_u^k(t) \rangle}{\lambda_{a_p^n}}. \quad (4.1)$$

Similarly, for estimation of the first two modes of the fast-varying symmetric mode subspace ( $\hat{s}_u^k$ ;  $k = 1$  and  $2$ ), associated with the second harmonics of the Kármán vortex shedding

$$\hat{s}_u^k(t_{est}) = \sum_{n=1}^2 s_p^n(t_{est} - \tau_s^n) \frac{\langle s_p^n(t - \tau_s^n) s_u^k(t) \rangle}{\lambda_{s_p^n}}. \quad (4.2)$$

For estimation of the slow-varying symmetric mode  $\hat{s}_u^\Delta$ , associated with the low-frequency dynamics, (2.17) is used.

Table 2 presents covariance magnitudes for the SPOD modes. Here, covariances between antisymmetric and symmetric modes are negligible. Covariances of higher-ranked pressure modes with the selected velocity modes were found to be similarly negligible.

For the antisymmetric field, covariances between modes associated with different frequencies in the velocity and pressure fields (e.g.  $a_u^3$  and  $a_p^1$ ) are not negligible. This is more noticeable when considering the covariance magnitudes for  $a_u^3$ ,  $a_u^4$ ,  $a_u^5$  and  $a_u^6$ . Therefore, for estimation of each antisymmetric SPOD modes, six pressure modes are considered. For  $\hat{a}_u^k$  ( $k = 1, 2, \dots, 6$ )

$$\hat{a}_u^k(t_{est}) = \sum_{n=1}^6 a_p^n(t_{est}) \frac{\langle a_p^n(t) a_u^k(t) \rangle}{\lambda_{a_p^n}}. \quad (4.3)$$

For the symmetric field, covariance magnitudes between modes corresponding to the low-frequency signature and second harmonics are negligible, which further reflects the separation of these dynamics using SPOD. Therefore, in estimating each symmetric SPOD mode, only the pressure modes yielding covariance coefficients above the threshold are considered. For modes associated with the low-frequency dynamics ( $\hat{s}_u^k$ ;  $k = 1$  and  $2$ )

$$\hat{s}_u^k(t_{est}) = \sum_{n=1}^2 s_p^n(t_{est} - \tau_s^n) \frac{\langle s_p^n(t - \tau_s^n) s_u^k(t) \rangle}{\lambda_{s_p^n}}. \quad (4.4)$$

For modes associated with the second harmonics of the Kármán vortex shedding ( $\hat{s}_u^k$ ;  $k = 3$  and  $4$ )

$$\hat{s}_u^k(t_{est}) = \sum_{n=3}^4 s_p^n(t_{est}) \frac{\langle s_p^n(t) s_u^k(t) \rangle}{\lambda_{s_p^n}}. \quad (4.5)$$

It is noted that the time delay  $\tau_a^n$  and  $\tau_s^n$  of (4.3) and (4.5) are smaller than the sampling interval and are thus omitted.

Figure 4 shows excerpts of time series of selected antisymmetric velocity POD/SPOD modes at  $z = 1.83$ . Actual and estimated temporal coefficients are shown by dashed blue and solid red lines, respectively. Table 3 presents the TKE contribution of the actual ( $\lambda_{a_u^i}$ ) and estimated ( $\lambda_{\hat{a}_u^i}$ ) modes.

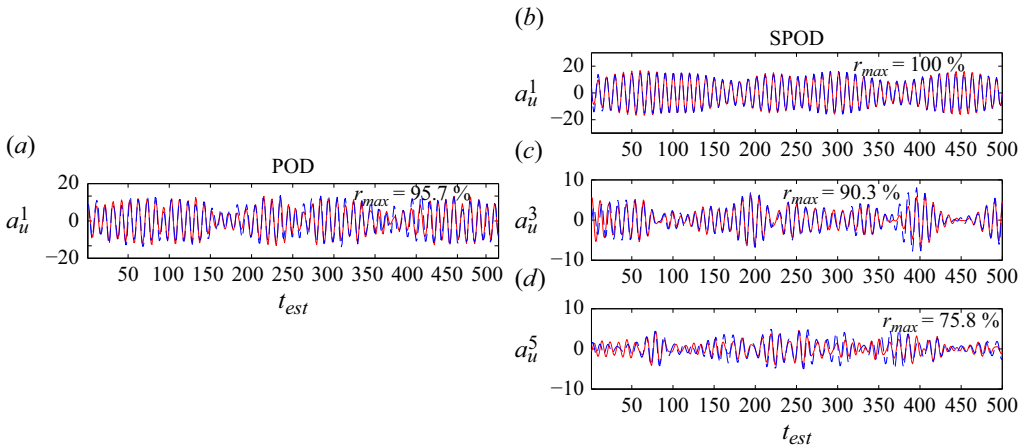


Figure 4. Comparison of actual (dashed blue,  $a_u$ ) and corresponding estimated (solid red,  $\hat{a}_u$ ) antisymmetric temporal coefficients at  $z = 1.83$ . Mode numbers correspond to the bases introduced in figure 2. Left side is with POD and right side is with SPOD. The reference pressure signal is naturally synchronized with the velocity data;  $\Delta(t_{est}) = 1/f_{PIV}$  throughout this study.

$n$	POD		SPOD	
	$\lambda_{a_u^n}(\%)$	$\lambda_{\hat{a}_u^n}(\%)$	$\lambda_{a_u^n}(\%)$	$\lambda_{\hat{a}_u^n}(\%)$
1	24.8	21.5	19.4	18.9
2	20.3	17.4	19.4	18.9
3			1.3	0.8
4			1.3	0.8
5			0.6	0.4
6			0.6	0.4
$\sum \lambda$	45.2	39.0	42.6	40.2

Table 3. Represented TKE ( $\lambda$ ) with the actual and estimated antisymmetric modes at  $z = 1.83$ . Magnitudes are rounded to the nearest decimal.

In figure 4, the phase of all temporal coefficients are well preserved. However, comparing figures 4(a) and 4(b),  $\hat{a}_u^1$  in SPOD more accurately represents  $a_u^1$ . The maximum cross-correlation magnitudes ( $r_{max}$ ), mentioned in the top right corner of each panel, is used as a coarse measure to assess the similarity between actual and estimated temporal coefficients. In figure 4(a),  $r_{max}$  is 95.7%, whereas in figure 4(b), it is near 100%.

Antisymmetric modes associated with the accompanying frequencies  $f_{ac1}$  and  $f_{ac2}$  can only be estimated with SPOD. With POD, the energetic contents around these frequencies are mixed with that of the primary shedding at  $f_s$  and therefore, the related dynamics cannot be estimated separately. With SPOD, however, a separate estimation of higher-ranked modes ( $\hat{a}_u^3$  to  $\hat{a}_u^6$ ), associated with  $f_{ac1}$  and  $f_{ac2}$ , is feasible. The correlations between corresponding actual and estimated temporal coefficients of these SPOD modes are lower than that of the first harmonic ( $r_{max}$  of 90.3% and 75.8% for  $a_u^3$  and  $a_u^5$ , respectively). Moreover, in figures 4(c) and 4(d), there are instances where the amplitude of  $a_u^3$  and  $a_u^5$  is not well captured by the corresponding estimated modes (e.g.  $350 < t_{est} < 400$ ). However, further investigation (presented later in this section) shows that the critical

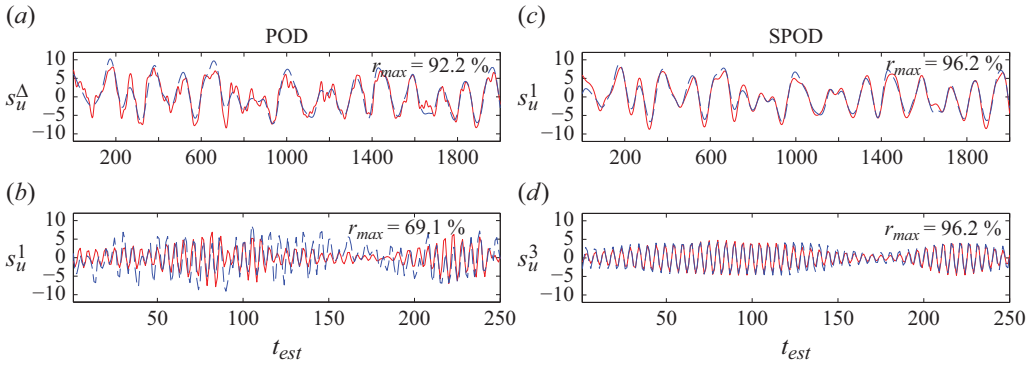


Figure 5. Comparison of actual (dashed blue,  $s_u$ ) and corresponding estimated (solid red,  $\hat{s}_u$ ) symmetric temporal coefficients at  $z = 1.83$ . Mode numbers correspond to the bases introduced in figure 2. Left side is with POD and right side is with SPOD. The reference pressure signal is naturally synchronized with the velocity data.

	POD		SPOD	
$n$	$\lambda_{s_u^n} (\%)$	$\lambda_{\hat{s}_u^n} (\%)$	$\lambda_{s_u^n} (\%)$	$\lambda_{\hat{s}_u^n} (\%)$
$\Delta$	2.6	3.0		
1	3.0	1.6	2.2	2.5
2	2.7	1.4	1.7	2.0
3			1.6	1.5
4			1.6	1.5
$\sum \lambda$	8.4	6.0	7.2	7.5

Table 4. Represented TKE ( $\lambda$ ) with the actual and estimated symmetric modes at  $z = 1.83$ . Magnitudes are rounded to the nearest decimal.

flow features (i.e. critical points and velocity gradients) are well preserved between the actual and estimated fields.

In table 3, the first two antisymmetric POD modes represent more TKE than the six selected SPOD modes (45.2 % vs. 42.6 %). However, for the estimated fields, more TKE is recovered with the selected SPOD basis (40.2 % vs. 39.0 % in POD), which is a result of high correlations between the actual and estimated temporal coefficients. The first two antisymmetric SPOD modes retain about 37.8 % TKE (out of 38.8 %) while the first two POD modes only retain 39.0 % TKE (out of 45.2 %). Including the TKE contributions retained by the other four estimated antisymmetric SPOD modes, associated with the accompanying frequencies, further favours the selection of SPOD over POD.

Figure 5 and table 4 present similar information to figure 4 and table 3, but for the symmetric field, at  $z = 1.83$ . In comparing the cumulative TKE contribution of symmetric modes associated with the slow-varying signature, the contribution of  $s_u^1$  and  $s_u^2$  of SPOD is higher than  $\hat{s}_u^\Delta$  of POD (3.9 % vs. 2.6 %). This is mainly attributed to a more successful separation of the low-frequency dynamics. For estimation of these modes, both POD- and SPOD-based techniques provide similar results, with the magnitude of  $r_{max}$  in figure 5(c) being 4 % higher than in figure 5(a). However, as a result of better separation of the dynamics with SPOD, the estimation of the two SPOD modes shows much less

high-frequency jitter (compare the smoothness of  $\hat{s}_u^\Delta$  in figure 5(a) and  $\hat{s}_u^1$  in figure 5(c) in the range  $1100 < t_{est} < 1200$ ).

Estimation of the modes representing the second harmonics of the Kármán vortex shedding ( $s_u^1$  and  $s_u^2$  with POD and  $s_u^3$  and  $s_u^4$  with SPOD) is significantly improved with SPOD. In figure 5(b), neither the pattern nor amplitude of the POD mode  $s_u^1$  is correctly captured by  $\hat{s}_u^1$ , which results in a relatively poor  $r_{max}$  of 69.1%. In comparison, in figure 5(d), the  $r_{max}$  between the SPOD mode  $s_u^3$  and its estimation  $\hat{s}_u^3$  is 96.2%, which is significantly higher. In terms of retaining TKE with the estimated modes (table 4), the POD modes  $\hat{s}_u^1$  and  $\hat{s}_u^2$  only retain 3.0% out of 5.7% TKE, whereas the SPOD modes  $\hat{s}_u^3$  and  $\hat{s}_u^4$  retain the same amount (3.0%), but out of 3.2% TKE. It should be re-iterated that the higher TKE contribution of the POD modes  $s_u^1$  and  $s_u^2$  compared with that of the SPOD modes  $s_u^3$  and  $s_u^4$  (5.7% vs. 3.2%) is mainly due to the low-frequency energy contents that are not separated from these POD modes (compare PSDFs of the POD mode  $s_u^1$  and SPOD mode  $s_u^3$  in figure 2).

Altogether, considering all five selected POD modes and ten selected SPOD modes, 45.0% TKE is recovered with the estimated POD modes (out of 53.6%) and 47.7% TKE is recovered with the estimated SPOD modes (out of 49.8%). Effectively, SPOD recovers more of the signal energy. Furthermore: (i) flow dynamics of the fundamental mode pair at  $f_s$  can be presented with less noise; (ii) weaker dynamics, such as the ones associated with the accompanying frequencies at  $f_{ac1}$  and  $f_{ac2}$ , can be estimated separately; and (iii) the modal dynamics associated with both low- and high-frequency energetic contents in the symmetric field is presented more accurately, especially in the case of the second harmonics of the Kármán vortex shedding.

Next, the quality of the estimated velocity modes, presented in figures 4 and 5, is further evaluated based on the residuals. Figure 6 presents the error of the instantaneous estimated velocity fields from partial reconstructions using POD (top) and SPOD (bottom) modes at  $z = 1.83$ . Similarly to Hosseini *et al.* (2015), the error is defined as

$$E_c = \frac{\int_y (\mathbf{u}_c - \hat{\mathbf{u}}_c) \cdot (\mathbf{u}_c - \hat{\mathbf{u}}_c) \, d\mathbf{A}}{\int_y \mathbf{u}_c \cdot \mathbf{u}_c \, d\mathbf{A}}, \quad (4.6)$$

where  $\mathbf{u}_c$  and  $\hat{\mathbf{u}}_c$  are the partial reconstruction using the actual and estimated modes, respectively, and the over-line denotes the time-averaging operator. In figure 6(a),  $E_c$  is the error between  $\mathbf{u}_c$  and  $\hat{\mathbf{u}}_c$ , reconstructed from the two antisymmetric modes and the mean field velocity. A lower  $E_c$  indicates a more accurate sensor-based estimation. The horizontal lines in figure 6 show the mean  $E_c$  value of the signal ( $\bar{E}_c$ ) in the same colour as the related  $E_c$  signal.

The  $\bar{E}_c$  of the SPOD reconstruction of the antisymmetric field (i.e.  $\mathbf{U} + \sum_{n=1}^6 a_u^n \phi_a^n$ ) is significantly lower than that of the corresponding POD reconstruction (0.03 vs. 0.11, as shown with horizontal black and red lines in figure 6(c) and figure 6(a), respectively). Considering contributions of individual antisymmetric SPOD mode pairs in figure 6(c), the  $E_c$  with higher-ranked mode pairs is higher (i.e. with  $\mathbf{U} + \sum_{n=1}^2 a_u^n \phi_a^n$ ,  $\mathbf{U} + \sum_{n=3}^4 a_u^n \phi_a^n$  and  $\mathbf{U} + \sum_{n=5}^6 a_u^n \phi_a^n$ ,  $\bar{E}_c \approx 0.01, 0.07$  and  $0.12$ , respectively), which will be shown in § 5 to reflect momentary intervals of disrupted vortex shedding. However, since the energetic contribution of the higher-ranked mode pairs are significantly lower than that of the first harmonic, the higher  $R_c$  of the modes associated with the accompanying frequency modes do not significantly affect the overall residual of  $\mathbf{U} + \sum_{n=1}^6 a_u^n \phi_a^n$ .

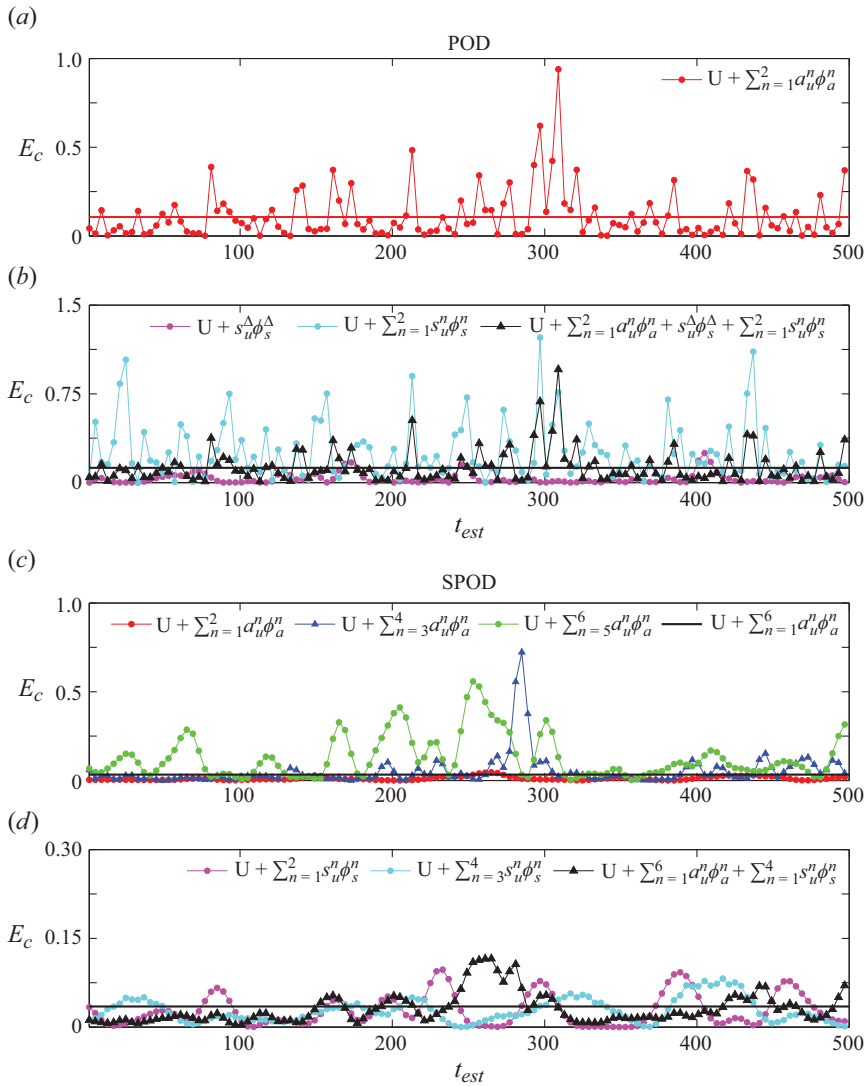


Figure 6. Error of the estimated velocity fields reconstructed using different selected POD ((a) and (b)) and SPOD ((c) and (d)) modes at  $z = 1.83$ . The horizontal lines show the average values in the same colour as the signal data points. The reference pressure data used for estimation are naturally synchronized (acquired simultaneously) with the velocity measurements. Note the difference between the vertical axes range.

For the symmetric field, reconstructions with slow-varying mode(s) (i.e.  $\mathbf{U} + s_u^\Delta \phi_s^\Delta$  with POD and  $\mathbf{U} + \sum_{n=1}^2 s_u^n \phi_s^n$  with SPOD),  $\overline{E}_c$  is low with both approaches (0.04 vs. 0.02, respectively). However, for the fast-varying modes associated with the second harmonics (i.e.  $\mathbf{U} + \sum_{n=1}^2 s_u^n \phi_s^n$  with POD and  $\mathbf{U} + \sum_{n=3}^4 s_u^n \phi_s^n$  with SPOD), the performance of the SPOD-based estimation is significantly better ( $\overline{E}_c \approx 0.25$  compared with 0.03). In figure 6(b),  $E_c$  magnitudes of  $\mathbf{U} + \sum_{n=1}^2 s_u^n \phi_s^n$  POD reconstruction are typically close or higher than 0.75, whereas they remain an order of magnitude smaller with the SPOD reconstruction  $\mathbf{U} + \sum_{n=3}^4 s_u^n \phi_s^n$  in figure 6(d) (note the difference in the vertical axes

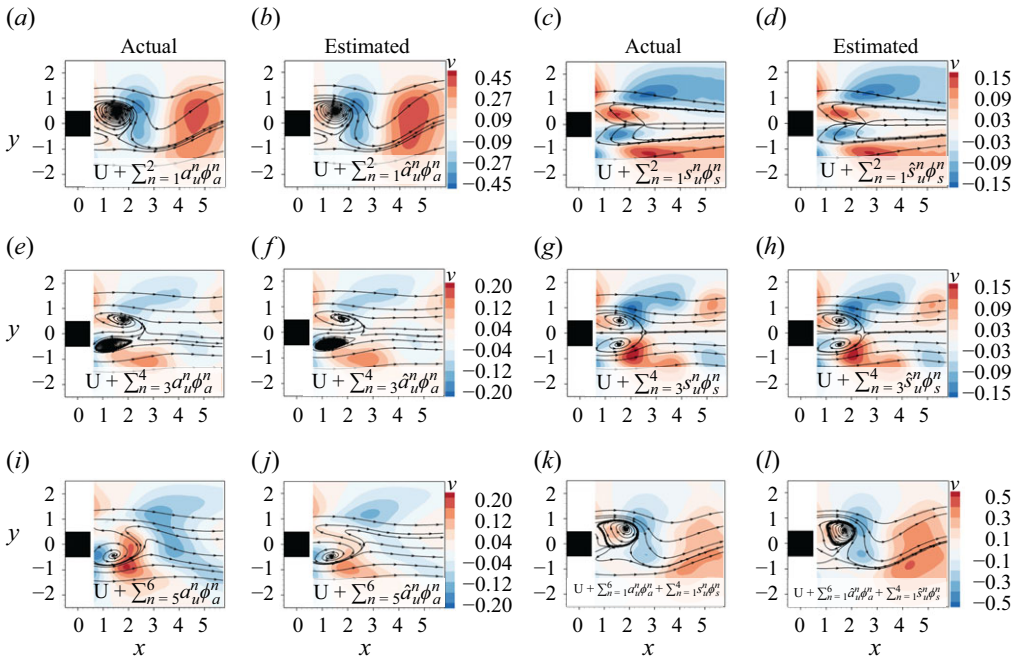


Figure 7. Iso-contours of the instantaneous lateral velocity component,  $v$ , overlaid with sectional streamlines at  $z = 1.83$ : columns 1 and 3 are reconstructions using selected SPOD modes; columns 2 and 4 show similar information with the estimated SPOD modes. All figures are plotted at the same time instant, corresponding to  $t_{est} = 500$  in figure 6. The same reference pressure data are used for estimation.

range between figures 6(b) and 6(d)). Finally, for reconstructions composed of all selected modes,  $\overline{E}_c$  for the POD modes is approximately 0.12, and nearly 4 times lower for SPOD.

Figure 7 shows iso-contours of  $v$ -component velocity, overlaid with sectional streamlines, from the measured (columns 1 and 3) and reconstructed (columns 2 and 4) flow fields at  $z = 1.83$  for a randomly selected PIV snapshot (POD reconstructions are not shown for brevity). The panels correspond to  $t_{est} = 500$  in figure 6. Supplementary video files no. 1 and no. 2 provide reconstructions corresponding to the data shown in figure 7.

In figure 7(k,l), the low-order reconstructions with all considered actual and estimated SPOD modes show very good similarity, both in terms of recovering the  $v$ -velocity contour patterns as well as type and location of streamline critical points. Similarly, a good agreement exists between the partial reconstructions with individual mode pairs. It is only in the case of the second pair of accompanying frequency mode pairs, figure 7(i,j), that discrepancies are easily observable between the reconstructions with actual and estimated modes, which is consistent with the results in figure 6(b). However, this has little effect when considering the reconstructions with all selected modes.

Figure 8 shows an example of the instantaneous relative reconstruction error map, corresponding to the instantaneous  $v$ -component velocity in figure 7, where the error parameter,  $E_v$ , is defined as

$$E_v = \sqrt{\frac{(v_c - \hat{v}_c)^2}{\mathbf{u}_c \cdot \mathbf{u}_c}}. \quad (4.7)$$

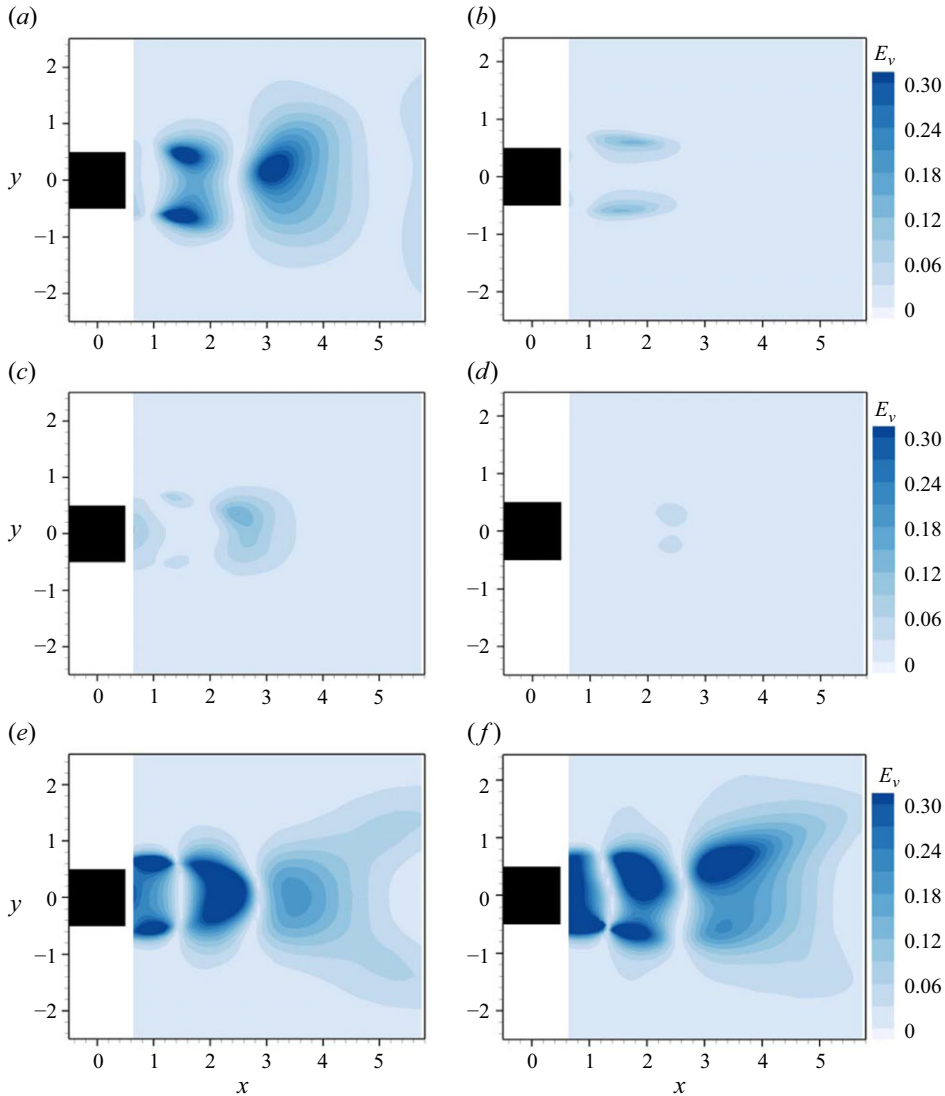


Figure 8. Error,  $E_v$ , between actual and estimated instantaneous  $v$ -component velocity, corresponding to the time instant shown in figure 7 (i.e.  $t_{est} = 500$  in figure 6). Panels (a), (b), (c), (d), (e) and (f) correspond to the  $E_v$  computed from figure 7(a)-(b), (c)-(d), (e)-(f), (g)-(h), (i)-(j) and (k)-(l), respectively.

For each panel of figure 8(a) to (e), the difference between partial reconstructions of the  $v$ -component velocity field using actual and estimated modes is shown. For example, figure 8(a) is obtained as the difference of  $v_c$  in figure 7(a) and  $\hat{v}_c$  in figure 7(b). Figure 8(f) shows the difference for the fields using the 10-mode reconstruction. For all panels,  $\mathbf{u}_c$  is the velocity field reconstructed from 10 actual modes.

In figure 8, high reconstruction errors occur in one of two scenarios: (i) when there is even a small difference between actual and estimated partial reconstructions of the most energetic coherent motion, such as the Kármán vortex shedding in figure 7(a) and (b) resulting in figure 8(a); and (ii) when there is a relatively large difference between the actual and estimated coefficients, even if the identified coherent motion is weak, such as  $(a_u^5, a_u^6)$  in figure 7(i) and (j) resulting in figure 8(e). It should be re-iterated that these

n	POD ( $z = 1.83$ )					SPOD ( $z = 1.83$ )				
	$\lambda_{a_u}^n$	$\lambda_{\hat{a}_u^n(1)}$	$\Delta\lambda_{a(1)}$	$\lambda_{\hat{a}_u^n(2)}$	$\Delta\lambda_{a(2)}$	$\lambda_{a_u}^n$	$\lambda_{\hat{a}_u^n(1)}$	$\Delta\lambda_{a(1)}$	$\lambda_{\hat{a}_u^n(2)}$	$\Delta\lambda_{a(2)}$
1	24.9	21.6	3.3	22.6	2.3	19.4	19.0	0.4	20.2	-0.8
2	20.3	17.4	2.9	18.3	2.0	19.4	19.0	0.4	20.2	-0.8
3						1.3	0.8	0.5	0.7	0.6
4						1.3	0.8	0.5	0.7	0.6
5						0.6	0.4	0.2	0.4	0.2
6						0.6	0.4	0.2	0.4	0.2
	$\lambda_{s_u}^n$	$\lambda_{\hat{s}_u^n(1)}$	$\Delta\lambda_{s(1)}$	$\lambda_{\hat{s}_u^n(2)}$	$\Delta\lambda_{s(2)}$	$\lambda_{s_u}^n$	$\lambda_{\hat{s}_u^n(1)}$	$\Delta\lambda_{s(1)}$	$\lambda_{\hat{s}_u^n(2)}$	$\Delta\lambda_{s(2)}$
$\Delta$	2.6	3.1	-0.5	1.9	0.7					
1	3.0	1.6	1.4	2.1	0.9	2.2	2.9	-0.7	1.9	0.3
2	2.7	1.4	1.3	1.9	0.8	1.7	2.0	-0.3	1.5	0.2
3						1.6	1.5	0.1	1.6	0.0
4						1.6	1.5	0.1	1.6	0.0
$\Sigma$	53.6	45.1		46.9		49.8	48.3		49.0	

Table 5. Relative TKE contribution (%) of temporal modes and their estimated counterparts at  $z = 1.83$ . Subscript (1) corresponds to the estimated coefficients obtained with synchronized pressure data (collected concurrently with the PIV measurements at  $z = 1.83$ ) and subscript (2) corresponds to the estimated coefficients obtained with asynchronous pressure data (collected concurrently with the PIV measurements at  $z = 0.92$ ).

panels are spatial distributions of the reconstruction error at a particular instant ( $t_{est} = 500$  in figure 6), which was chosen to represent a high error level case of the full reconstruction. As can be seen from the sample time interval in figure 6, the error in the full reconstruction is generally significantly smaller than at these extreme instants. Notwithstanding, the error levels are generally less compared with the ones reported in other studies, for example by Deng *et al.* (2019).

In this section, the performance of the SPOD-based sensor estimation technique was compared with the POD-based counterpart. The reference pressure data were naturally synchronized (acquired concurrently) with the PIV measurements. However, in cases where a 3-D velocity field is to be reconstructed from individual uncorrelated (acquired at different times) planar velocity measurements, a common reference pressure signal needs to be used to synchronize the 3-D estimation. Therefore, the next section will focus on evaluating the performance of the proposed methodology when reconstructing the flow using data from uncorrelated planes.

#### 4.2. Estimation results using asynchronous pressure data

This section starts with a comparison between estimated temporal coefficients at  $z = 1.83$ , obtained using synchronized and un-synchronized reference pressure data. Then, the estimated signals with asynchronous data are analysed at other heights. For all estimations with the asynchronous pressure data, the reference pressure acquired concurrently with the PIV measurements at  $z = 0.92$  is used to estimate the velocity at all other planes.

Table 5 presents relative TKE contribution (%) of selected POD/SPOD modes at  $z = 1.83$  and their estimated counterparts obtained using (i) synchronized pressure data (similar to the data presented in table 3) and (ii) asynchronous pressure data (collected concurrently with the PIV measurements at  $z = 0.92$ ). The difference between the TKE of the estimated and actual modes are presented by  $\Delta\lambda_{a/s(1)}$  and  $\Delta\lambda_{a/s(2)}$ . The focus is on evaluating the estimator performance in retaining TKE when asynchronous pressure data are used for estimation.

From table 5, in general, the SPOD-based technique retains more TKE of the original signal. For the fundamental harmonic coefficient  $\hat{a}_u^1$ ,  $\Delta\lambda_{a(1)}$  and  $\Delta\lambda_{a(2)}$  are approximately 3.3 % and 2.3 % with POD, whereas they are 0.4 % and (-0.8) % with SPOD, respectively. The higher magnitudes of  $\lambda_{\hat{a}_u^1(2)}$  compared with that of  $\lambda_{\hat{a}_u^1(1)}$  with both POD and SPOD reflect a more energetic reference pressure signal in group (2), which is obtained with PIV measurements at  $z = 0.92$ , compared with that of group (1). Differences between different realizations (trials) of the pressure sequences are within the statistical uncertainty as discussed in Appendix B. A similar pattern is seen for  $\hat{a}_u^2$ . For the accompanying frequency modes, the quality of the SPOD estimator does not change significantly using asynchronous reference pressure data (i.e. for  $\hat{a}_u^3$  to  $\hat{a}_u^6$ ,  $\Delta\lambda_{a(1)} \approx \Delta\lambda_{a(2)}$ ).

For symmetric modes, the performance of the POD and SPOD-based estimators do not change significantly using the asynchronous reference pressure signal. For the low-frequency modes, the performance is similar between both estimators. For the estimation of the second harmonics of the Kármán vortex shedding, however, the performance of the SPOD-based estimator remains significantly better than the POD-based estimator, using the asynchronous reference pressure signal. Appendix B presents a complementary discussion on the effect of using different sensor data on retaining modal TKE.

To further explore the quality of estimation with POD and SPOD-based techniques, the dynamical (phase) relationship is considered. Figure 9 depicts phase portraits of selected actual (rows 1 and 3) and estimated (rows 2 and 4) coefficients. The phase portraits in the first three columns show data over approximately 250 shedding cycles. The  $x$ -axis corresponds to  $a_u^1$  (rows 1 and 3) and  $\hat{a}_u^1$  (rows 2 and 4). The temporal coefficients for the  $y$ -axis were selected illustrating relationships with  $a_u^1$ . Similar patterns are observed with both POD and SPOD temporal coefficients: in (a) and (i), the cyclical relationship between the two modes of a harmonic pair is resolved; in (b) and (j), the parabolic relationship between the shedding strength and the slow-varying component is rendered (Noack *et al.* 2003; Bourgeois *et al.* 2011); and in (c) and (k), Lissajou portraits are seen, which indicate that the phase dynamics of the  $2f_s$  harmonic is enslaved to the fundamental harmonic (Bourgeois *et al.* 2013). The trajectories are clearer in the SPOD case, especially with retaining the Lissajou patterns, figure 9(o), which is a result of improved separation of the flow dynamics.

The last column of figure 9 presents the phase relationship for a short excerpt of the time series (covering about four shedding cycles) of temporal coefficients associated with the second harmonics of Kármán vortex shedding ( $\{s_u^1, s_u^2\}$  with POD and  $\{s_u^3, s_u^4\}$  with SPOD). Ideally, the modes corresponding to the second harmonics should exhibit a cyclical relationship, similar to that of the first (fundamental) mode pair. However, the expected cyclical pattern is not resolved in the POD case. In contrast, the cyclical pattern is very well preserved with SPOD (figure 9(l) and figure 9(p)) by using only the linear terms, as in (4.5). Furthermore, with SPOD, the estimated coefficients of the second harmonics are already in phase with those of the first, such that the delay  $\tau_s^n = 0$ , unlike with POD where the delay is needed. Therefore, the SPOD-based estimation is more successful in preserving the phase-relations between modes.

The performance of the SPOD-based estimator in capturing the modal energy content when using asynchronous reference pressure signals is discussed next. Figure 10(a) shows variation of the TKE contribution of the five most energetic actual SPOD mode pairs relative to the TKE of all modes in each plane. Briefly,  $\lambda_a^1 + \lambda_a^2$  relates to  $f_s$ ,  $\lambda_a^3 + \lambda_a^4$  to  $f_{ac1}$ ,  $\lambda_a^5 + \lambda_a^6$  to  $f_{ac2}$ ,  $\lambda_s^1 + \lambda_s^2$  to  $f_L$  and  $\lambda_s^3 + \lambda_s^4$  to  $2f_s$ . The contribution of  $\lambda_a^1 + \lambda_a^2$  is dominant for  $z \leq 2.05$ . Above  $z > 2.05$ ,  $\lambda_s^1 + \lambda_s^2$  notably increases and  $\lambda_a^1 + \lambda_a^2$  notably decreases, such that for  $z > 3$ , the low-frequency  $f_L$  motion, originating at the obstacle's

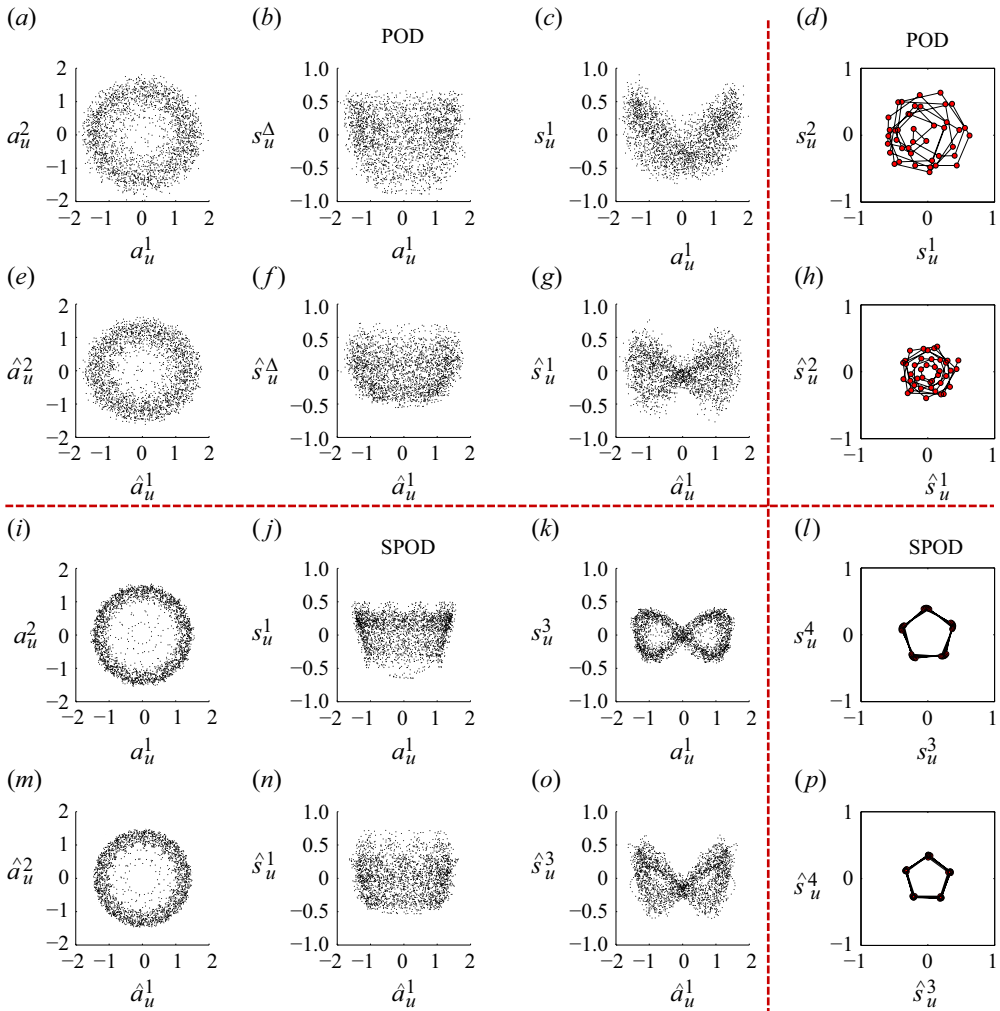


Figure 9. Phase portraits of selected actual (rows 1 and 3) and estimated (rows 2 and 4) temporal coefficients: rows 1 and 2 are with POD and rows 3 and 4 are with SPOD. Mode numbers correspond to the bases introduced in figure 2. For the last column, only a short excerpt of the time series (covering about four shedding cycles) are shown for better visualization. Note that with POD,  $\{s_u^1, s_u^2\}$  and  $\{\hat{s}_u^1, \hat{s}_u^2\}$ , and with SPOD,  $\{s_u^3, s_u^4\}$  and  $\{\hat{s}_u^3, \hat{s}_u^4\}$  are related to the second harmonics of Kármán vortex shedding.

free end, dominates the vortex shedding signature. The variations of  $\lambda_a^3 + \lambda_a^4$  and  $\lambda_a^5 + \lambda_a^6$  closely follow each other. For  $z \leq 2.05$ , the relative TKE contributions of both mode pairs stay nearly constant; for  $2.05 < z \leq 2.75$ , they increase with strengthening of the low-frequency instability; and for  $z > 2.75$ , they decrease following the weakening of the Kármán vortex shedding. Lastly,  $\lambda_s^3 + \lambda_s^4$  is strongest in the  $1.25 < z < 3$  region, which coincides with the loci of streamwise vortical connector strands (Mohammadi *et al.* 2022). These flow patterns will be explained in greater details in § 5.

Figure 10(b) shows the absolute magnitudes of TKE contribution of the converged SPOD modes (from six trials). Figure 10(c) shows similar information for the estimated coefficients using the asynchronous pressure data, measured concurrently with the PIV measurements at  $z = 0.92$  based on a single trial. The two plots are not overlaid for clarity. It can be seen that the TKE distributions are similar for the estimated and converged set of

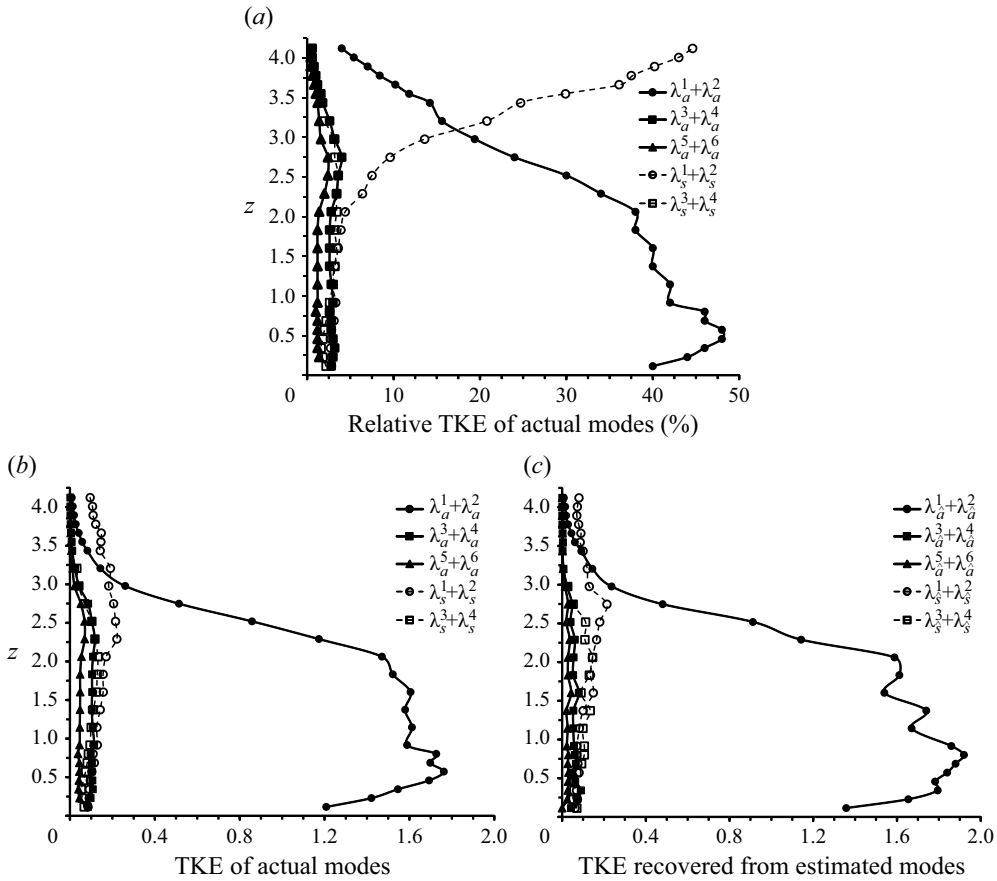


Figure 10. (a) Actual (measured) energy content of SPOD modes relative to TKE (%); (b) TKE of actual SPOD modes; and (c) TKE recovered of SPOD modes. Here,  $\lambda_a^1 + \lambda_a^2$  corresponds to  $f_s$ ,  $\lambda_a^3 + \lambda_a^4$  to  $f_{ac1}$ ,  $\lambda_a^5 + \lambda_a^6$  to  $f_{ac2}$ ,  $\lambda_s^1 + \lambda_s^2$  to  $f_L$  and  $\lambda_s^3 + \lambda_s^4$  to  $2f_s$ .

actual SPOD modes along the cylinder height. However, due to the stochastic nature of the flow during separate measurements, differences exist between the two sets. In Appendix B, TKE contributions from a converged dataset and from single trials are further compared.

Figure 11 presents estimated temporal coefficients at  $z = 0.46$  (left side) and  $2.75$  (right side). The root mean square (r.m.s.) of each signal is shown at the top right corner of each panel. It can be seen that the amplitude (strength) and r.m.s. of the  $\hat{a}_u^1$  coefficient are significantly smaller at  $z = 2.75$  compared with  $z = 0.46$ . In contrast, the amplitude and r.m.s. of  $\hat{s}_u^1$  are significantly larger at  $z = 2.75$  compared with  $z = 0.46$ . In comparison, those of  $\hat{a}_u^3$ ,  $\hat{a}_u^5$  and  $\hat{s}_u^3$  do not show significant changes between the two planes. These observations are consistent with the TKE magnitudes presented in figure 10(c).

It should be clarified that for estimations using asynchronous pressure data, any other reference pressure data (acquired concurrently with PIV measurements at any other heights) could be used. Several tests with other reference pressure data verified that the estimated signals capture the patterns of actual temporal coefficients and correctly retain the TKE of SPOD modes at every other plane. The choice of using the pressure data acquired concurrently with PIV measurements at  $z = 0.92$  (among some others),

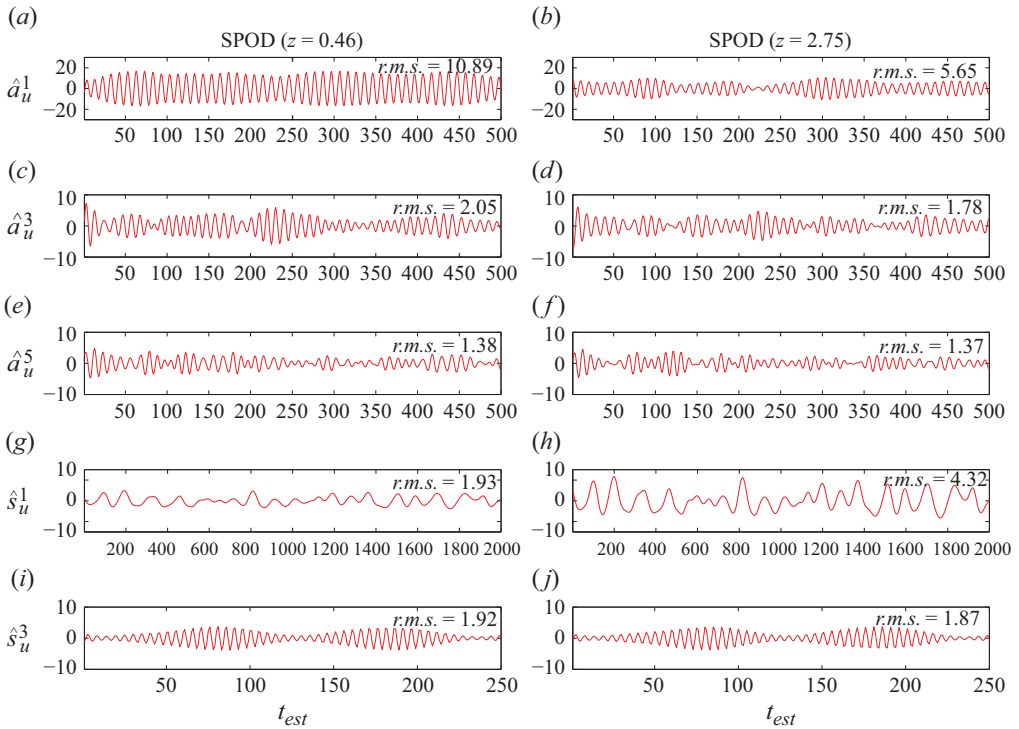


Figure 11. Estimated SPOD temporal coefficients at  $z = 0.46$  (left side) and  $2.75$  (right side), calculated using a reference pressure, synchronized with the PIV measurements at  $z = 0.92$ . Mode numbers correspond to the bases introduced in figure 2.

however, made it possible to capture unique 3-D physical phenomena which will be further discussed in § 5.

## 5. Results – 3-D reconstruction of the estimated instantaneous velocity field

This section starts with a summary of the mean and phase-averaged flow fields from Mohammadi *et al.* (2022) to introduce the characteristic features of the near wake of the cantilevered square cylinder to provide a context for this study. Then, a 3-D reconstruction of the instantaneous velocity field, based on the estimated planar velocity fields, is presented and analysed. The flow field is estimated using a common reference pressure signal measured concurrently with the PIV measurements at  $z = 0.92$ .

### 5.1. Mean and phase-averaged 3-D velocity fields

Figure 12 shows educed mean vortex structures as rendered by  $Q = 0$  criterion ( $Q \geq 0$  identifies vortex core following Hunt *et al.* (1978)), coloured by streamwise vorticity,  $\Omega_x$ . Two pairs of streamwise vortices, dipole ( $D^{+/-}$ ) (Wang *et al.* 2006; Bourgeois *et al.* 2011; Hosseini *et al.* 2013) and descending vortices ( $DV^{+/-}$ ) (Kindree *et al.* 2018), extend from the mean lee-ward recirculation region. These vortex pairs have the same sense of rotation on each side of the symmetry plane ( $y = 0$ ), and were shown to be separate structures (Kindree *et al.* 2018; Mohammadi *et al.* 2022).

The dipole and descending vortices are the mean signature of half-loop vortex shedding pattern downstream of the vortex formation region (Bourgeois *et al.* 2011; Mohammadi

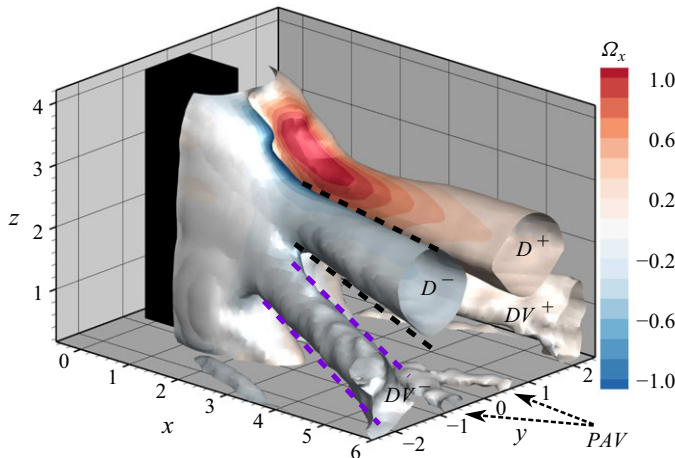


Figure 12. Educated mean vortex structures identified by the  $Q = 0$  criterion and coloured by streamwise vorticity,  $\Omega_x$ : black and purple dashed lines correspond to the dipole ( $D^{+/-}$ ) and descending vortices ( $DV^{+/-}$ ), respectively. Dashed arrows indicate an additional pair of post attachment vortices ( $PAV$ ), which were related to interactions of the horse-shoe vortex system and Kármán vortices (Mohammadi *et al.* 2023). Figure is reprinted with permission from Mohammadi *et al.* (2022).

*et al.* 2022). Mohammadi *et al.* (2022) elucidated the vortex topology from the 3-D phase-averaged reconstruction of the flow field. Figure 13(left side) shows phased-averaged iso-surfaces of  $Q = 0$  at three shedding phases,  $\phi_1$ ,  $\phi_3$  and  $\phi_{10}$ , covering half of the shedding cycle. Figure 13(right side) shows the vortex skeleton schematics inspired by these educated vortex structures. The phase-averaged shedding cycle is rendered in the supplementary video file no. 3.

In figure 13(a) and figure 13(b), phase  $\phi_1$ , the top of recently shed vortex  $A$  bends upstream, forming a strand connecting to the incipient forming vortex  $A^+$  at the obstacle base. This strand induces a downwash along  $y = 0$ . On the opposing side, vortex  $B$  is developing in the base region. Vortex  $B^-$  has shed from the previous half-cycle and its associated strand has already rotated inward and connected with vortex  $A$ , in the region indicated with a blue dashed circle. By phase  $\phi_3$ , figure 13(c) and figure 13(d), the half-loop pattern connecting vortices  $A$  and  $B^-$  is more clearly defined. The connector strand of vortex  $A$  is still connected to vortex  $A^+$ , but at a lower elevation. Its axis has rotated towards vortex  $B$ , which has grown considerably. As vortex  $B$  begins to shed ( $\approx \phi_5$ ), vortex  $A$  completely detaches from vortex  $A^+$  and forms a half-loop with vortex  $B$ . Note that during this process ( $\phi_1$  to  $\phi_{10}$ ), the strand remains located within the bounds of the mean dipole (indicated by the black dashed lines) and the connection site remains within the bounds of the descending vortices (indicated by the purple dashed lines). This supports the interpretation that the dipole and descending vortices of figure 12 are the mean signature of the instantaneous half-loop shedding pattern in figure 13.

The phase-averaged reconstruction provides cycle-resolved representation of the coherent motions occurring at a certain frequency, in this case the average shedding frequency,  $f_s$ , and its harmonics. Consequently, contributions of coherent motions at other frequencies are smeared in the averaging process and their influence is not captured. Hence, the phase average represents the vortex topology during a typical shedding cycle, as can be seen in the reconstructions using the present estimation (see supplementary video file no. 3). In the present flow, however, the vortex shedding process is highly modulated and contributions of coherent motions occurring at other frequencies are

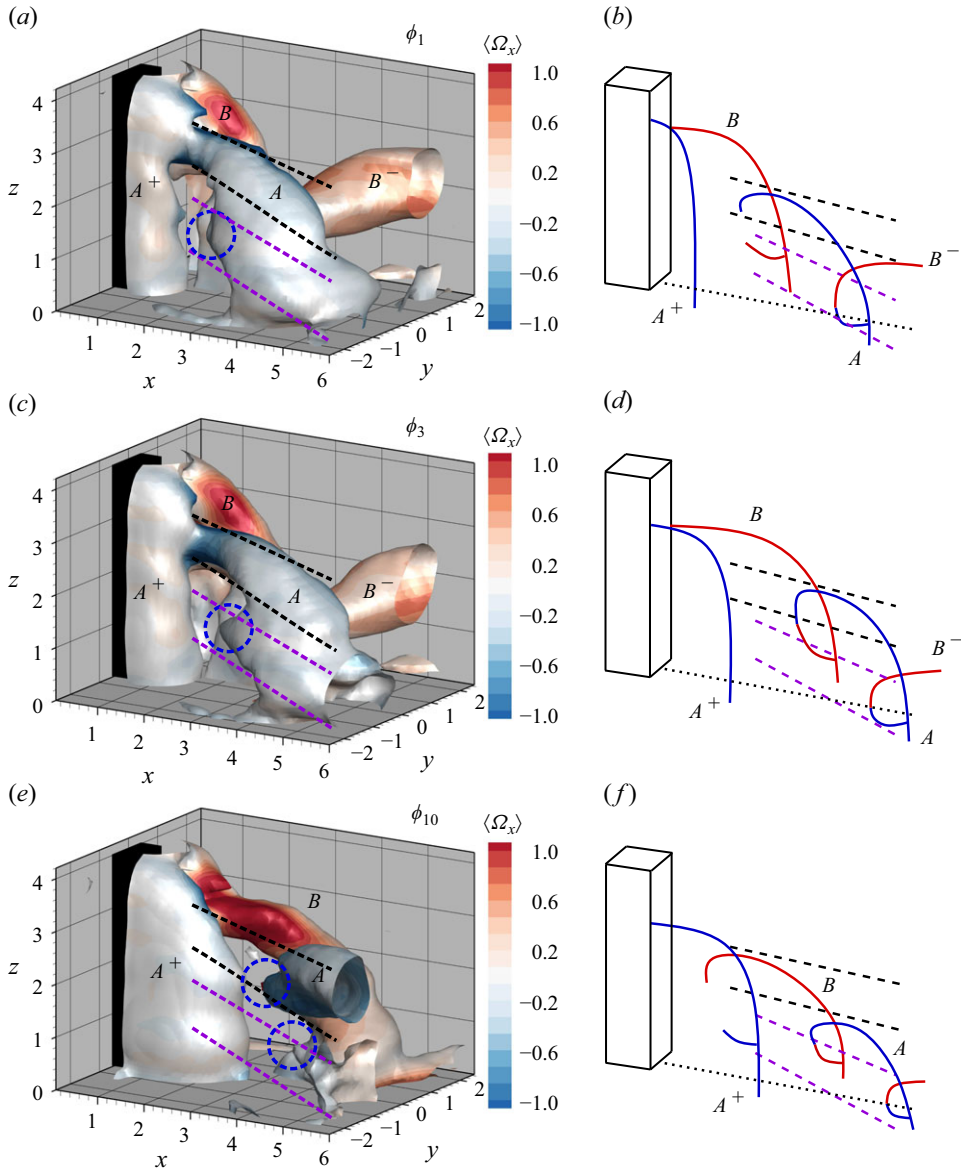


Figure 13. Left side: educed phased-averaged vortex structures identified by the  $Q = 0$  criterion and coloured by streamwise vorticity,  $\langle \Omega_x \rangle$ , at phases (a)  $\phi_1$ , (c)  $\phi_3$  and (e)  $\phi_{10}$ , where  $\phi_n = \phi_0 + n\pi/10$  (with an arbitrary  $\phi_0$ ). The dashed lines are the bounds of the dipole and descending vortices as shown in figure 12. Right side: vortex skeleton schematics, inspired by the educed vortex structures on the left.

expected to be important. In the following section, it will be shown that estimator-based 3-D reconstruction of the flow field makes it possible to study the cycle-to-cycle variations.

### 5.2. Instantaneous 3-D reconstruction of the flow field

Figure 14 shows the temporal coefficients of velocity modes in the  $z = 1.83$  plane estimated using reference pressure data collected concurrently with the PIV measurements at  $z = 0.92$ . The temporal coefficients are ordered based on increasing TKE contribution

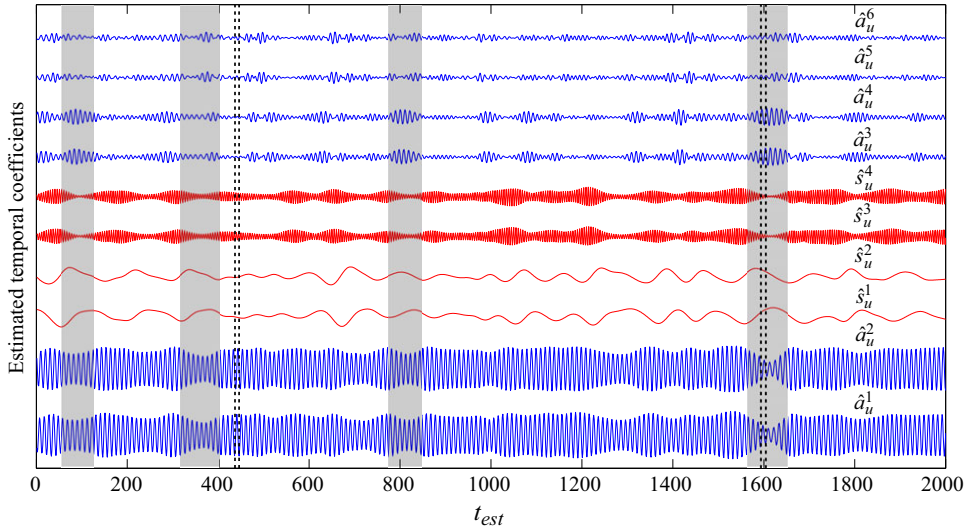


Figure 14. Time series of estimated temporal coefficients at  $z = 1.83$  using asynchronous pressure data (collected concurrently with PIV measurements at  $z = 0.92$ ). Estimated temporal coefficients are ordered from bottom to top based on their TKE contribution. Antisymmetric and symmetric modes are coloured in blue and red, respectively. Four intervals are coloured in grey, reflecting regions where the Kármán vortex shedding is modulated: for  $70 < t_{est} < 130$ ,  $\hat{s}_u^1$  and  $\{\hat{a}_u^3, \hat{a}_u^4\}$  are strong; for  $320 < t_{est} < 400$ ,  $\{\hat{s}_u^1, \hat{s}_u^2\}$  is strong, but  $\{\hat{a}_u^3, \hat{a}_u^4\}$  is weak; for  $780 < t_{est} < 840$ ,  $\{\hat{a}_u^3, \hat{a}_u^4\}$  is strong, but  $\{\hat{s}_u^1, \hat{s}_u^2\}$  is weak; and for  $1550 < t_{est} < 1650$ , both  $\{\hat{s}_u^1, \hat{s}_u^2\}$  and  $\{\hat{a}_u^3, \hat{a}_u^4\}$  are strong. Intervals between the two sets of dashed lines ( $437 < t_{est} < 446$  and  $1594 < t_{est} < 1605$ ) indicate a typical and an atypical vortex shedding period, respectively.

from bottom to top. For clarity, temporal coefficients of the antisymmetric and symmetric SPOD modes are coloured in blue and red, respectively.

In figure 14, the amplitude of the temporal coefficients show significant cycle-to-cycle variation. Closer inspection suggests amplitude changes for different coefficients coincide. For instance, the variations of the signal amplitude envelope of the second harmonics of the Kármán vortex shedding,  $\{\hat{s}_u^3, \hat{s}_u^4\}$ , generally follow those of the fundamental harmonics  $\{\hat{a}_u^1, \hat{a}_u^2\}$  (e.g. amplitudes in regions coloured in grey). Also, generally, the first pair of the accompanying frequency modes,  $\{\hat{a}_u^3, \hat{a}_u^4\}$ , seems to be more active (amplitudes increase) when the low-frequency modes  $\{\hat{s}_u^1, \hat{s}_u^2\}$  are stronger. Note that  $\hat{s}_u^2$  lags  $\hat{s}_u^1$  for approximately  $2/f_L$  or  $1/5 f_s$  (see Appendix C for a discussion on the difference between  $s_u^1$  and  $s_u^2$ ).

The variations of the strength (amplitude) of the fundamental harmonic of Kármán vortex shedding,  $\{\hat{a}_u^1, \hat{a}_u^2\}$ , seem related to the strength of low-frequency modes,  $\{\hat{s}_u^1, \hat{s}_u^2\}$ , and the first pair of the accompanying frequency modes,  $\{\hat{a}_u^3, \hat{a}_u^4\}$ . Generally, three main patterns can be identified in figure 14:

- (i) The Kármán vortex shedding is similar to a typical cycle when neither  $\{\hat{a}_u^3, \hat{a}_u^4\}$  nor  $\{\hat{s}_u^1, \hat{s}_u^2\}$  is strong, such as the shedding period between the dashed lines about  $t_{est} \approx 440$ .
- (ii) The Kármán vortex shedding is weakly modulated under three circumstances:
  - (a)  $\{\hat{a}_u^3, \hat{a}_u^4\}$  and one of the  $\hat{s}_u^1$  or  $\hat{s}_u^2$  modes are strong (e.g. the grey interval about  $t_{est} \approx 100$ );
  - (b)  $\{\hat{s}_u^1, \hat{s}_u^2\}$  is strong, but  $\{\hat{a}_u^3, \hat{a}_u^4\}$  is weak (e.g. the grey interval about  $t_{est} \approx 360$ ); and
  - (c)  $\{\hat{s}_u^1, \hat{s}_u^2\}$  is weak, but  $\{\hat{a}_u^3, \hat{a}_u^4\}$  is strong (e.g. the grey interval about  $t_{est} \approx 810$ ).

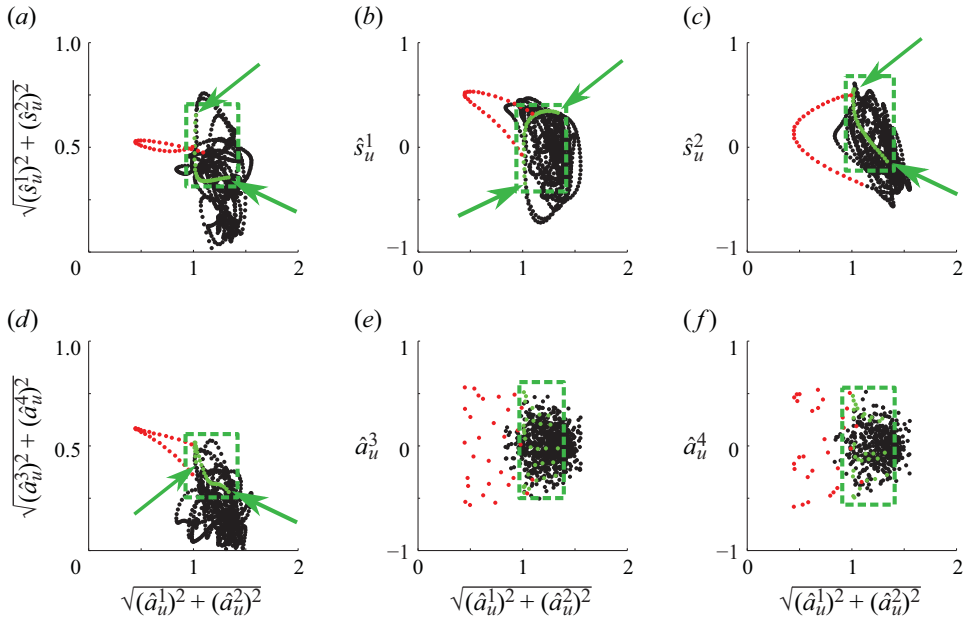


Figure 15. Phase plots of selected estimated temporal coefficients and envelopes of the amplitudes of selected mode pairs, all against the envelope of the first harmonic temporal coefficients, at  $z = 1.83$ . Estimated coefficients are obtained using asynchronous reference pressure signal (i.e. collected concurrently with PIV measurements at  $z = 0.92$ ). Green and red data points correspond to the first ( $70 < t_{est} < 130$ ) and last ( $1550 < t_{est} < 1650$ ) grey regions in figure 14, respectively. Green dashed boxes and green arrows are added to help visualizing the bounds of the data points in the first interval. Every second point is plotted for clarity.

- (iii) The Kármán vortex shedding is strongly modulated (nearly suppressed) when both  $\{\hat{s}_u^1, \hat{s}_u^2\}$  and  $\{\hat{a}_u^3, \hat{a}_u^4\}$  are strong, such as the interval within the dashed lines about  $t_{est} \approx 1600$ .

Figure 15 shows phase plots of temporal coefficients corresponding to the low-frequency signature  $\{\hat{s}_u^1, \hat{s}_u^2\}$ , first pair of accompanying frequency modes  $\{\hat{a}_u^3, \hat{a}_u^4\}$ , and the corresponding amplitude envelope for each pair (i.e.  $\sqrt{(\hat{s}_u^1)^2 + (\hat{s}_u^2)^2}$  and  $\sqrt{(\hat{a}_u^3)^2 + (\hat{a}_u^4)^2}$ , respectively), all against the envelope for the first harmonics of Kármán vortex shedding (i.e.  $\sqrt{(\hat{a}_u^1)^2 + (\hat{a}_u^2)^2}$ ). Most data points fall in a dense cluster.

Data points lying on trajectories outside the cluster can typically be related to changes in modulation or the dynamics of the vortex shedding. In figure 15, two groups of data points are distinguished: (i) the green-coloured data points are related to the weakly modulated motions in the first grey interval ( $70 < t_{est} < 130$ ) in figure 14, and (ii) the red-coloured data points are related to the nearly suppressed cycles in the last grey interval ( $1550 < t_{est} < 1650$ ) in figure 14. To help identifying the bounds of the first group data points, green dashed boxes and green arrows are added. The second group data points are generally on the left side of the green dashed boxes. For the first group, although the magnitude of  $\sqrt{(\hat{s}_u^1)^2 + (\hat{s}_u^2)^2}$  can go as high as approximately 0.70 in figure 15(a), the magnitude of  $\sqrt{(\hat{a}_u^1)^2 + (\hat{a}_u^2)^2}$  remains above 1, indicating only a weak modulation to the Kármán vortex shedding. In this interval, most of the contributions to  $\sqrt{(\hat{s}_u^1)^2 + (\hat{s}_u^2)^2}$  come from  $\hat{s}_u^1$  while  $\hat{s}_u^2$  remains about zero (see figure 15(b) and figure 15(c) and the time series of figure 14). For the second group, on the other hand, while  $\sqrt{(\hat{s}_u^1)^2 + (\hat{s}_u^2)^2}$

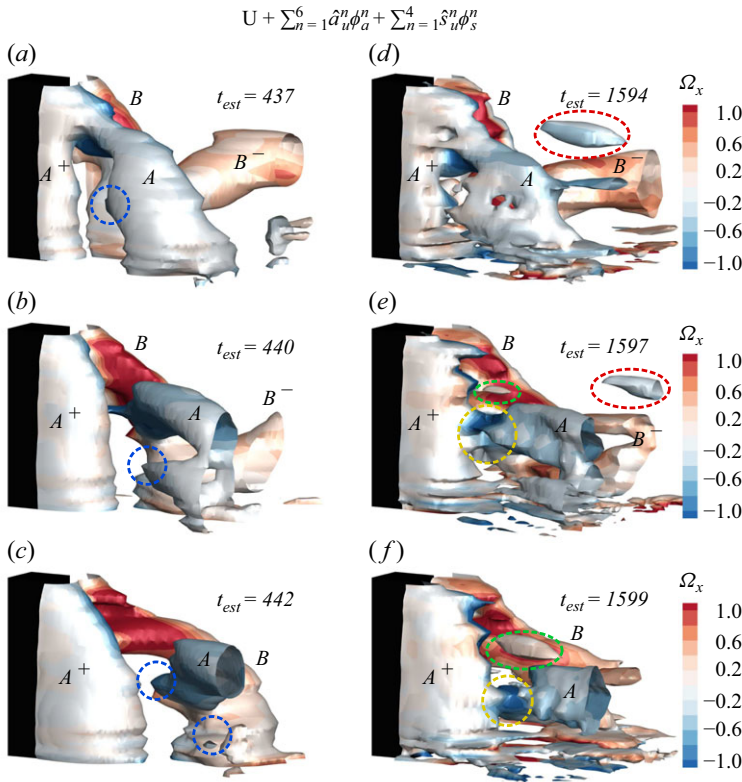


Figure 16. Educated vortex structures, using  $Q = 0$  criterion, from reconstruction of the flow field with all 10 SPOD velocity modes. Iso-surfaces are coloured with streamwise vorticity,  $\Omega_x$ . Both time intervals shown on the left and right sides cover approximately half of the shedding cycles, indicated with dashed lines in figure 14. The beginning of these cycles are selected such that they correspond to the phase-averaged reconstruction of phase  $\phi_1$  in figure 13. For (a)–(c), added annotations are similar to those of figure 13 (left side). For (d)–(e), the enclosed regions with yellow dashed-lines indicate loci of un-conventional re-attachments of connector strands. Regions indicated with green and red dashed lines indicate patched of isolated vortices, originating from near the free end.

hovers around 0.5 in figure 15(a),  $\sqrt{(\hat{a}_u^1)^2 + (\hat{a}_u^2)^2}$  reach very low magnitudes, indicating a significant modulation of the the Kármán vortex shedding. During this interval, both  $\hat{s}_u^1$  and  $\hat{s}_u^2$  contribute similarly to  $\sqrt{(\hat{s}_u^1)^2 + (\hat{s}_u^2)^2}$ , which indicates that for the Kármán vortex shedding to be suppressed, both low-frequency modes must be strong. Additionally, during the suppressed cycles, the amplitude envelope of  $\hat{a}_u^3$  and  $\hat{a}_u^4$  (i.e.  $\sqrt{(\hat{a}_u^3)^2 + (\hat{a}_u^4)^2}$  in figure 15(d)) is larger when compared with the weakly modulated cycles.

Typical and very strongly modulated (atypical) vortex shedding cycles are compared next. Figure 16 shows educated vortex structures, using the  $Q = 0$  criterion, from a reconstruction of the flow field using the 10 estimated SPOD velocity modes. Three instances of two time intervals indicated with dashed lines in figure 14 are shown:  $437 \leq t_{est} \leq 442$  (typical) and  $1594 \leq t_{est} \leq 1599$  (atypical). In general, the typical shedding cycles last between 9 and 10 time units to complete, whereas the atypical shedding cycles during the  $1550 < t_{est} < 1650$  interval take between 10 and 12 time units. The cycles shown in figure 16 take 10 and 11 time units, respectively. Thus, the shown time intervals in both cases cover approximately half of a shedding cycle. For the first interval (typical cycle), the low frequency and first accompanying frequency mode pairs are weak, whereas

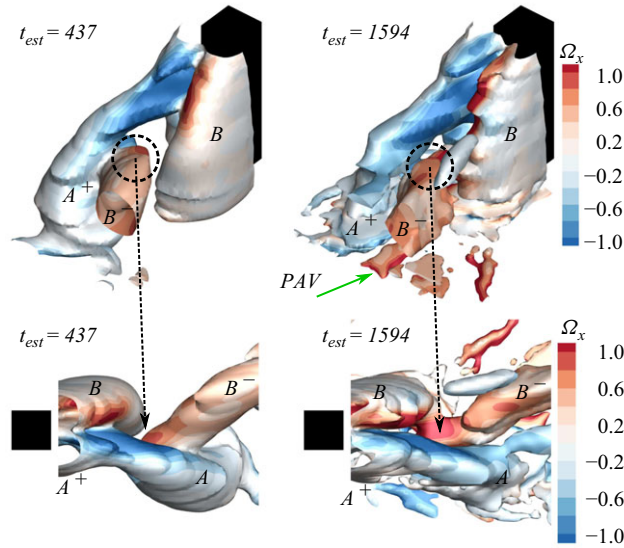


Figure 17. Educated vortex structures, using  $Q = 0$  criterion, from reconstruction of the flow field with all 10 SPOD velocity modes. Iso-surfaces are coloured with streamwise vorticity,  $\Omega_x$ . For the plots on left, the time instance is the same as in the figure 16(a) and for the plots on right, the time instance is the same as in the figure 16(d). Annotations in black colour indicate the connection sites between Kármán vortices, and the green arrow indicate the structure associated with post attachment vortices (PAV) in figure 12.

for the second interval (atypical cycle), both these mode pairs are strong. Supplementary video files no. 4 to no. 7 show the flow field reconstruction for  $0 < t_{est} < 2000$  (over 200 shedding cycles); each file covers 500 time units. Additionally, figure 17 shows the educated vortex structures of figure 16(a) and figure 16(d) from two other angles; figure 18 shows iso-contours of reconstructed  $\hat{v}$ - and  $\hat{w}$ -velocity components from reconstructions of figure 16, overlaid by sectional pseudo-streamlines, at the symmetry plane ( $y = 0$ ); and figure 19 shows similar information to figure 18 at two horizontal planes,  $z = 1$  and  $z = 2$ .

The iso-surfaces in figure 16(a–c) capture the educated vortex structures during  $437 \leq t_{est} \leq 442$ . During this typical cycle, the educated Kármán vortex shedding patterns are very similar to the phase-averaged reconstructions of figure 13. In the half-loop shedding pattern shown in figure 16(a–c), the top of a newly shed Kármán vortex  $A$  detaches from  $A^+$ , re-orientates towards the symmetry plane and connects with the back side of a newly formed Kármán vortex  $B$  on the opposite side. This connection to the opposite side vortex can be better seen in figure 17(left side), which shows the half-loop pattern formed between vortices  $B^-$  and  $A$  at  $t_{est} = 437$  (same as in figure 16(a)).

In figure 18, the pseudo-saddle points, indicated by green arrows, show the loci of intersection between two positive bifurcation surfaces: one originating from the top of the cylinder and the other originating from the base plate. For the first interval, figure 18(left side), the position of this saddle point moves between  $z = 0.75$  and  $1.75$ , which is consistent with its mean location during a phase-averaged cycle, at approximately  $z \approx 1.25$ . Furthermore, the iso-contour patterns of  $\hat{v}$ -velocity component in figure 18(a<sub>1</sub>) and (b<sub>1</sub>) are similar to the ones obtained from the phase-averaged field (Mohammadi *et al.* 2022).

The educated vortical structures for the atypical shedding cycle during  $1594 \leq t_{est} \leq 1605$ , figure 16(d–f), are significantly different from either the phase-averaged or typical

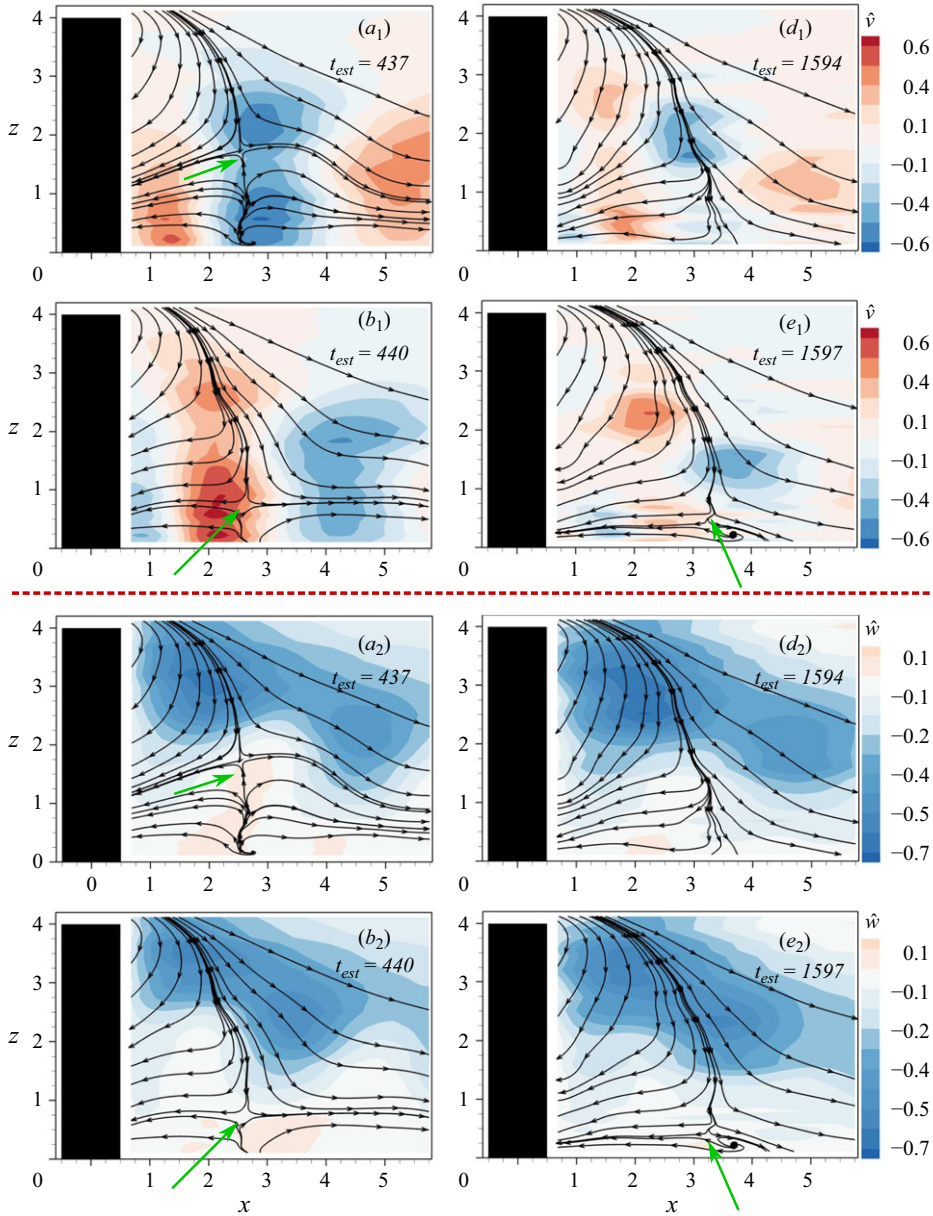


Figure 18. Iso-contours of  $\hat{v}$ - and  $\hat{w}$ -velocity components from reconstructions shown in figure 16, overlaid with sectional pseudo-streamlines at the symmetry plane ( $y = 0$ ). Green arrows indicate pseudo-saddle points. For better correspondence between two figures, letter (c) is not used in addressing the panels.

cycle reconstructions. This is associated with (i) an increase in the amplitudes of  $\{\hat{\delta}_u^1, \hat{\delta}_u^2\}$ , which are related to the low-frequency ( $f_L$ ) motion from the obstacle's free end, and (ii) an increase in the strength of interactions between the  $f_L$  motion and Kármán vortex shedding ( $f_S$ ), which is reflected in the amplitude of coefficients of the first pair of accompanying frequencies  $\{\hat{a}_u^3, \hat{a}_u^4\}$ . As a result, the first and second harmonics of the Kármán vortex shedding become weak (see associated time series in figure 14), the connector strands form at a lower spanwise location (i.e. top of vortex A in figure 16(d) is at  $z = 2.7$  compared

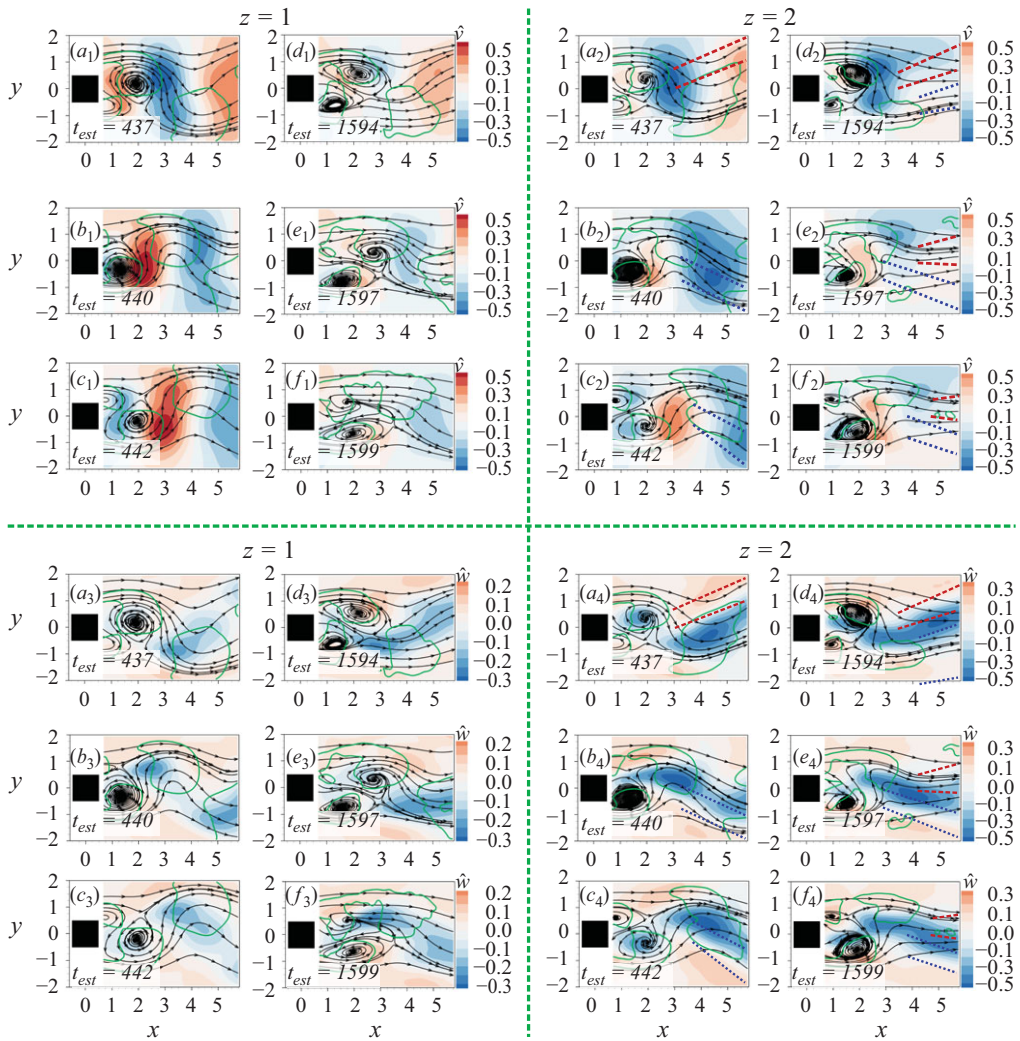


Figure 19. Iso-contours of reconstructed velocity components using all 10 selected SPOD modes. Quadrant one (top left) shows  $\hat{v}$ -component at  $z = 1$ , quadrant two (top right)  $\hat{v}$ -component at  $z = 2$ , quadrant three (bottom left)  $\hat{w}$ -component at  $z = 1$ , and quadrant four (bottom right)  $\hat{w}$ -component at  $z = 2$ . The iso-contours are overlaid with sectional pseudo-streamlines and iso-contours of  $Q = 0.01$  (solid green lines). Additionally, at  $z = 2$ , the bounds of connector strands intersections with the plane are indicated using dashed and dotted lines, where the line colours indicate the sense of rotation of streamwise vorticity,  $\Omega_x$ , of the strand. Time stamps are the same as in figure 16.

with that in figure 16(a) at  $z = 3.2$ ), and the associated shedding process (i.e. half-loop shedding pattern) is strongly disrupted, giving rise to regions of vortex dislocation. Here, the backward-tilted top of vortex  $A$  remains connected to the newly forming Kármán vortex on the same side, vortex  $A^+$  (see regions enclosed by yellow dashed lines in figure 16(e) and 16(f)). While this connection moves to lower heights as the shedding cycle continues, it does not re-orient towards the symmetry plane to connect with vortex  $B$ . As a result, the so-called half-loop shedding pattern does not form. This vortex connection pattern is further visualized in figure 17(right side), which shows the connection formed between vortices  $B^-$  and  $B$  at  $t_{est} = 1594$  (same as in figure 16(d)).

This disrupted vortex formation pattern is accompanied by another pair of streamwise vortices, originating from close to the free end of the obstacle. In [figure 16\(e\)](#), the vortex core, enclosed with a green dashed line, has an opposite sense of rotation to the primary vortex and associated connector strand below it. As the shedding process goes on, this vortex core grows (see [figure 16\(f\)](#)), without connecting with the vortical strands below it. Similarly, on the opposite side of [figures 16\(d\)](#) and [16\(e\)](#), growing vortex cores with an opposite sign of streamwise vortices to the connector strands below them, are enclosed with red dashed lines.

The difference in the orientation of the connector strands between the typical and atypical cycles becomes more clear in comparing [figure 19\(a<sub>2</sub>\)-\(c<sub>2</sub>\)](#) with [figure 19\(d<sub>2</sub>\)-\(e<sub>2</sub>\)](#), where the connectors strands intersections with the horizontal plane at  $z = 2$  are indicated with red (dashed) and blue (dotted) lines. The line colours reflect the sign of streamwise vorticity of the vortical strand (red, positive and blue, negative). It can be seen that during  $437 \leq t_{est} \leq 442$ , only one vortical strand intersects with the  $z = 2$  plane. For instance, at  $t_{est} = 437$ , only the red-coloured connector strand (originating from positive  $y$  values) crosses the mid-span height, which connects with the opposite Kármán vortex at lower heights. At this time instance, another blue-coloured connector strand is forming, but is still at higher elevations (see [figure 16\(a\)](#)). During  $1594 \leq t_{est} \leq 1599$ , on the other hand, although the newer connector strand (the one closer to the obstacle in each time instance) is located at slightly higher  $z$  position compared with the older one, the difference in their spanwise location is small, such that both intersect with the  $z = 2$  plane at all time instances. The simultaneous presence of these vortical strands around the mid-height of the obstacle induces a strong downwash about the symmetry plane, as evident in [figure 19\(d<sub>4</sub>\)-\(f<sub>4</sub>\)](#), which further dislocates the Kármán vortex structures in the lower half of the wake. These observations are consistent with the differences in iso-contours of  $\hat{v}$ - and  $\hat{w}$ -velocity components in [figure 18](#).

Finally, the stronger negative  $\hat{w}$ -component velocity in the lower half of the obstacle during the atypical cycle alters the topology of streamlines in the symmetry plane. The pseudo-saddle point mentioned earlier in the discussion of [figures 18\(a<sub>1</sub>\)](#) and [18\(a<sub>2</sub>\)](#), is not detected in [figures 18\(d<sub>1</sub>\)](#) and [18\(d<sub>2</sub>\)](#). Instead, the positive bifurcation line from the free end extends all the way to the base plate. Additionally, in comparison with [figures 18\(b<sub>1</sub>\)](#) and [18\(b<sub>2</sub>\)](#), the saddle point in [figures 18\(d<sub>1</sub>\)](#) and [18\(d<sub>2</sub>\)](#) is at a significantly lower location ( $z \approx 0.35$  compared with 0.75) and a more advanced streamwise position ( $x \approx 3.4$  compared with 2.6), which indicates a longer recirculation region in the atypical case. The location of this saddle point downstream of the mean recirculation length coincides with the beginning of a  $\Lambda$ -shaped mean structure observed over the base plate ( $x > 4$ ,  $-1 < y < 1$ ) in [figure 12](#). This structure was associated with intermittent interactions between Kármán vortices and the horse-shoe vortex system (Mohammadi *et al.* 2023), which is partly captured in [figure 17](#)(right side).

## 6. Concluding remarks

In this study, the FIR-SPOD of Sieber *et al.* (2016) was implemented in the sensor-based multi-time-delay estimation technique of Hosseini *et al.* (2013). This approach simplifies the process of obtaining reliable correlations between pressure and velocity modes. It is found that the dynamic relationships between coherent motions in different PIV planes are better retained, resulting in improved estimation and reconstruction of the 3-D dynamics. The diagnostic case used for implementation of this technique was the highly modulated, quasi-periodic turbulent wake of a cantilevered square cylinder with  $h/d = 4$ , immersed in a thin laminar boundary layer ( $\delta/d = 0.21$ ) at  $Re = 10600$ . It was shown that, through

a precise rendering of the estimated 3-D velocity field, intervals of vortex shedding interruption and vortex dislocations events were captured, thus allowing investigations of cycle-to-cycle variations.

The estimation methodology of Hosseini *et al.* (2015) heavily relied on a careful selection and construction of orthonormal velocity and pressure fields. While the POD-based multi-time-delay estimation is successful in rendering the most energetic coherent dynamics, such as the first harmonic of the Kármán vortex shedding and low-frequency signature from the obstacle's free end using linear terms, it performs poorly in estimating higher-ranked modes. Hosseini *et al.* (2015) suggested that the mode pair containing second harmonics could be better estimated using a quadratic relation with the pressure modes. While this approach did slightly improve the estimation of the second harmonic modes, benefits to the estimation of other modes are less evident.

Here, the ability of FIR-SPOD in yielding modes with better spectral separation is leveraged to simplify and generalize the process of finding reliable correlations between velocity and pressure modes, without the need to implement additional filtering to distil a particular motion, or to involve nonlinear relationships between different modes. The accuracy of estimations were assessed using both synchronous and asynchronous reference pressure data, where significant improvements were achieved over the POD space. In particular, some important motions or modes could be explicitly estimated, which was not possible with POD. These modes are very important for describing the interactions and distortions of the shedding cycle. Furthermore, with the FIR-SPOD technique, the behaviour of the original signal, phase relationships between different coefficients, and the TKE contribution of individual modes, were better retained, and the instantaneous estimation error was reduced significantly. The planar reconstruction of the flow fields using estimated signals verified that both the velocity patterns and critical points of the flow compare well with the ones obtained from actual PIV measurements.

The benefits of this approach are highlighted through the 3-D instantaneous reconstruction of the estimated flow field using the selected FIR-SPOD modes. Through this presentation, the cycle-to-cycle variations can be investigated. For example, intervals of interrupted vortex shedding were rendered in the near wake of the candidate flow. It was shown that the half-loop shedding pattern (Bourgeois *et al.* 2011, 2013; Hosseini *et al.* 2015; Mohammadi *et al.* 2022) was interrupted and no longer formed, mainly as a result of strong downwash from the free end and modulations of the vortex strand interactions with the Kármán vortices. During these intervals, as a result of the imposed vortex dislocations, connector strands between the Kármán vortices on the opposite sides do not reconnect with the opposing vortex. Instead, the primary body of a suppressed Kármán vortex tilts backwards and connects with the successive Kármán vortex on the same side. Additional investigations between a typical and an interrupted shedding cycle through the time series analysis confirmed that complete suppression of Kármán vortex shedding can occur during such intervals.

The proposed methodology is a significant step towards a relatively straightforward but powerful and reliable estimation of planar velocity fields and correcting phase relationships between uncorrelated PIV planes, which leads to reconstruction of the global dynamics. Through such visualizations, instantaneous patterns would emerge which are not possible using a phase-averaging process, where the cycle-to-cycle variations of the dominant dynamics is masked. Through a reliable interpretation of the weaker dynamics (higher-ranked modes), instantaneous variations of the dominant motions could be more easily and confidently studied. Furthermore, the technique makes it possible to further explore the contributions of individual modes in the development of the flow physics and investigate the global relationships between different coherent motions.

**Supplementary materials.** Supplementary materials are available at <https://doi.org/10.1017/jfm.2025.93>.

**Acknowledgments.** The authors gratefully acknowledge the funding support from the Natural Sciences and Engineering Research Council of Canada (NSERC) through the Collaborative Research & Development (CRD), Research Tools and Instrumentation (RTI) and Discovery Grant (DG) programs. We also gratefully acknowledge the funding support from the University of Calgary through the Faculty of Graduate Studies Doctoral Scholarship, Ruby Doctoral Scholarship, Graduate Studies Scholarship and ASME Pipeline Systems Division Award.

**Declaration of interests.** The authors report no conflict of interests.

### Appendix A. Orthogonality of SPOD spatial modes

The ability of SPOD to deliver a more refined dynamics and separate frequencies within narrow spectral bandwidth comes at the expense of spatial orthogonality. SPOD spatial modes,  $\tilde{\Psi}$ , are only orthonormal if they are considered with all of the temporally shifted instances

$$\frac{1}{M} \sum_{l=-N_f}^{N_f} \tilde{\Psi}_i(x_k, \tau_l) \tilde{\Psi}_j(x_k, \tau_l) = \delta_{ij} . \quad (A1)$$

In the snapshot SPOD for the velocity field, however, the modal decomposition is only feasible for time-independent spatial modes (i.e.  $\tau = 0$ ). Therefore, the resulting modes are neither normal nor orthogonal

$$\frac{1}{M} \sum_{k=1}^M \Psi_i(x_k) \Psi_j(x_k) \neq \delta_{ij} . \quad (A2)$$

Sieber *et al.* (2016) argued that the most energetic modes are almost orthogonal. Table 6 presents the magnitude of inner products of the selected SPOD modes in this study (i.e. six antisymmetric and four symmetric modes) with the selected modes of their respective subspace. Note that since the data in each part of the table are symmetric, the data points above the diagonals are replaced with a hyphen (-). It can be seen that for the first four antisymmetric and the first four symmetric modes, the inner product magnitudes are small. It is only with the  $\phi_a^5$  and  $\phi_a^6$  that the inner product magnitude increases, indicating a decrease in the angle between two spatial modes, which result in an incomplete representation of the original data in flow reconstructions.

Nevertheless, Sieber *et al.* (2016) further argued that the missing part of each SPOD mode in reconstruction (due to non-orthogonality) is completed by considering its mode pair, which in most cases (i.e. depending on the selected filter length), has a similar energy content to the first mode. Therefore, a suitable selection of the filter length and considering both modes of each considered mode pair compensates for the non-orthogonality effects, at least for the dominant coherent structures. Readers are referred to the original work of Sieber *et al.* (2016) for a more complete discussion and illustrative examples.

### Appendix B. Effect of using different sensor data on TKE of estimated coefficients

In § 4.2, it was mentioned that using either synchronous or asynchronous pressure data provide satisfactory results in terms of retaining TKE of the actual modes, where the performance was improved with the SPOD technique. The difference between  $\Delta\lambda_{a/s(1)}$  and  $\Delta\lambda_{a/s(2)}$  was mainly related to the difference between the fluctuating energy of

$(\phi_a^i, \phi_a^j)$	$\phi_a^1$	$\phi_a^2$	$\phi_a^3$	$\phi_a^4$	$\phi_a^5$	$\phi_a^6$	$(\phi_s^i, \phi_s^j)$	$\phi_s^1$	$\phi_s^2$	$\phi_s^3$	$\phi_s^4$
$\phi_a^1$	1.0	-	-	-	-	-	$\phi_s^1$	1.0	-	-	-
$\phi_a^2$	0.01	1.0	-	-	-	-	$\phi_s^2$	-0.03	1.0	-	-
$\phi_a^3$	0.09	0.04	1.0	-	-	-	$\phi_s^3$	0.01	-0.04	1.0	-
$\phi_a^4$	0.15	0.23	0.27	1.0	-	-	$\phi_s^4$	-0.11	0.17	-0.01	1.0
$\phi_a^5$	0.66	0.34	0.15	0.41	1.0	-					
$\phi_a^6$	0.28	-0.67	-0.23	-0.06	0.01	1.0					

Table 6. Inner products of SPOD spatial modes at  $z = 1.83$ . Repetitive data are replaced with a hyphen (-) for visualization purposes.

$n$	All Trials	Trial 1		Trial 2		Trial 3		Trial 4		Trial 5		Trial 6	
	$\lambda_{a_p}^n$	$\lambda_{a_p}^n$	$\Delta\lambda_{a_p}^n$										
1	24.7	25.5	-0.8	22.9	1.8	25.9	-1.3	23.6	1.1	24.2	0.5	26.5	-1.8
2	24.7	25.5	-0.8	22.9	1.8	25.9	-1.3	23.6	1.1	24.2	0.5	26.5	-1.8
3	1.9	1.6	0.3	2.4	-0.5	1.7	0.2	2.3	-0.3	1.7	0.2	1.5	0.4
4	1.9	1.6	0.3	2.4	-0.5	1.7	0.2	2.3	-0.3	1.7	0.2	1.5	0.4
5	0.8	0.8	0.1	1.0	-0.2	0.9	0.0	0.9	0.0	0.8	0.0	0.6	0.2
6	0.8	0.8	0.1	1.0	-0.2	0.9	0.0	0.9	0.0	0.8	0.0	0.6	0.2
$n$	$\lambda_{s_p}^n$	$\lambda_{s_p}^n$	$\Delta\lambda_{s_p}^n$										
	1	3.3	2.6	0.7	4.1	-0.8	2.8	0.5	3.5	-0.2	3.8	-0.6	3.1
2	2.4	2.0	0.4	2.6	-0.2	2.1	0.3	2.6	-0.2	2.9	-0.5	2.2	0.2
3	2.9	3.0	-0.2	2.5	0.4	2.7	0.1	2.7	0.1	3.0	-0.2	3.2	-0.3
4	2.9	3.0	-0.2	2.5	0.4	2.7	0.1	2.7	0.1	3.0	-0.2	3.2	-0.3

Table 7. Comparison of TKE contribution (%) of different pressure modes, obtained from performing SPOD on individual trials and all six trials. Data are obtained concurrently with PIV measurements at  $z = 0.92$ .

reference pressure data, used for estimation. Here, this statement is considered more closely.

Table 7 presents the TKE contributions of pressure modes from performing SPOD on individual trials and complete set of trials of pressure data, obtained concurrently with PIV measurements at  $z = 0.92$ . The difference between the TKE contribution of each mode, obtained from each individual trial and the complete set is shown by  $\Delta\lambda$ . It can be seen that the TKE contribution of modes differ from that of the converged set (i.e. all trials). This observation reflects the stochastic nature of the flow, where for each trial or realization, the TKE and relative modal contributions to the TKE differ. However, the differences are within the statistical uncertainty estimate for random error and as mentioned in the text, when four or more trials are used for obtaining the SPOD modes, the results converge (see Appendix B of Mohammadi *et al.* (2023)). This clarification should help in better understanding the difference between  $\Delta\lambda_{a/s(1)}$  and  $\Delta\lambda_{a/s(2)}$ , presented in table 5. A similar discussion can be made for the velocity modes, but is not presented for brevity.

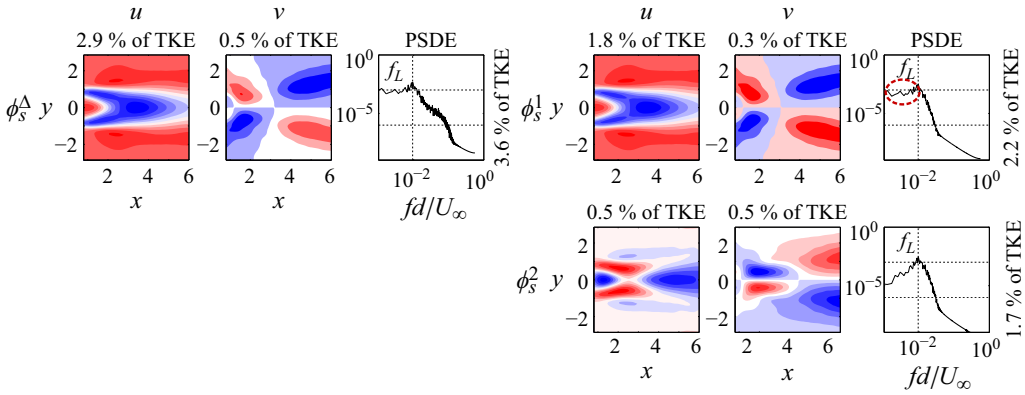


Figure 20. Velocity modes associated with the low-frequency signature at  $z = 1.83$ : left side ( $\phi_s^\Delta$ ) is with POD and right side ( $\phi_s^1$  and  $\phi_s^2$ ) are with SPOD ( $N_f = 64$ ).

### Appendix C. Relationship between the low-frequency symmetric SPOD modes

In § 5.2, it was mentioned that although both SPOD modes  $s_u^1$  and  $s_u^2$  present a low-frequency nature, they are not quite the same. Here, this statement will be investigated more closely. Note that a similar discussion can be presented for the pressure modes  $s_p^1$  and  $s_p^2$ , but is not done for brevity.

Figure 20 illustrates the  $u$  and  $v$  spatial functions of the POD (left side:  $\phi_s^\Delta$ ) and SPOD (right side:  $\phi_s^1$  and  $\phi_s^2$ ) modes associated with the low-frequency signature at  $z = 1.83$ . To the right of each set, the PSDF of each mode is shown. It can be seen that the spatial distribution of the  $\phi_s^\Delta$  and  $\phi_s^1$  are very similar, but their modal TKE (defined as the TKE of each respective mode) is different (i.e. 3.6 % vs. 2.2 %). Despite this difference, the TKE portion of different components are relatively similar. For both modes, the  $u$  component constitutes approximately 81 % of the modal TKE (i.e. 2.9 % with  $\phi_s^\Delta$  and 1.8 % with SPOD), whereas the  $v$  and  $w$  components (the latter is not shown for brevity) constitute approximately 14 % and 5 % of the modal TKE, respectively. Therefore, it can be concluded that  $\phi_s^\Delta$  and  $\phi_s^1$  represent the same dynamics.

The SPOD  $\phi_s^2$ , however, exhibits different behaviour than SPOD  $\phi_s^1$  (and POD  $\phi_s^\Delta$ ) in three respects: (i) distribution of different spatial components, (ii) TKE ratio of different components, where  $u$  and  $v$  components constitute approximately 30 % of the modal TKE and  $w$  component constitutes approximately 40 % of the modal TKE and, most importantly, (iii) distribution of PSDF. Comparing the PSDF of SPOD modes  $\phi_s^1$  and  $\phi_s^2$ , it can be seen that spectral contents with frequencies less than  $f_L$  are much more energetic in  $\phi_s^1$ . This region is indicated with a red dashed oval in the PSDF of  $\phi_s^1$ .

To investigate the difference between  $\phi_s^1$  and  $\phi_s^2$ , figure 21 illustrates the scatter plots of time series (a)  $s_u^2$  vs.  $s_u^1$ , (b)  $s_u^1$  vs.  $a_u^1$  and (c)  $s_u^2$  vs.  $a_u^1$ . In figure 21(a), a clear cyclical pattern exists between  $s_u^1$  and  $s_u^2$ , which suggests that they constitute a mode pair at a frequency  $f_L$ . However, due to the lower-frequency ( $< f_L$ ) energetic contents present in  $\phi_s^1$ , there are some off-cycle behaviour as well. Therefore, mode  $\phi_s^1$  can be considered as a mixture of a slow-varying motion (Bourgeois *et al.* 2013; Hosseini *et al.* 2016) with frequencies less than  $< f_L$  and a cyclical motion centred at  $f_L$ , which is also present in  $\phi_s^2$ . Consistently, the scatter plot of  $s_u^1$  vs.  $a_u^1$  forms a parabolic shape in figure 21(b), similar

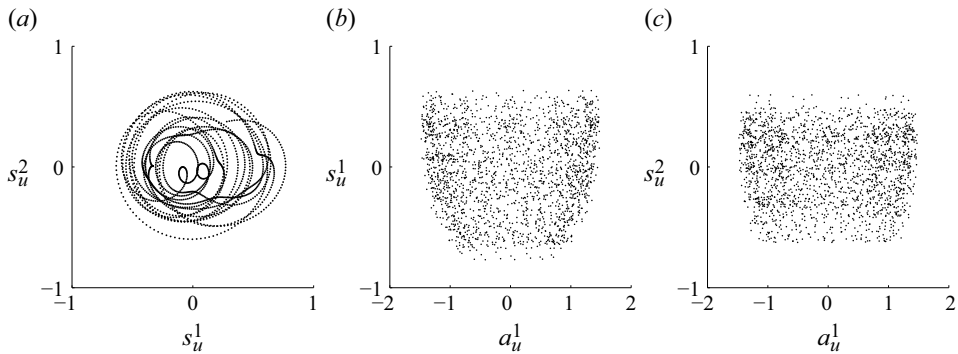


Figure 21. Scatter plots of selected SPOD temporal coefficients: (a) the second low-frequency mode ( $s_u^2$ ) vs. the first low-frequency mode ( $s_u^1$ ); (b)  $s_u^1$  vs. the first antisymmetric mode ( $a_u^1$ ), associated with the Kármán vortex shedding; and (c)  $s_u^2$  vs.  $a_u^1$ .

to the ones reported for a slow-varying signature making modulations to the fundamental harmonics in highly modulated wake regions (Bourgeois *et al.* 2013; Hosseini *et al.* 2016). This pattern is not seen between  $s_u^2$  and  $a_u^1$  in figure 21(c), which is attributed to the less energetic presence of the slow-varying components (with frequencies below  $f_L$ ) in  $s_u^2$ .

#### Appendix D. Lobe patterns

In implementing the multi-time-delay technique to the pressure data, a lobe pattern is observed in the spectra of the pressure POD modes. Since the reconstruction of the velocity modes is based directly on the pressure modes, the dynamics of the estimated field will contain artefacts (the lobes). With SPOD, regardless of the number of virtual sensors or the sampling frequency, the lobe patterns are not observed. Figure 22 depicts the PSDF of POD modes obtained from the pressure matrix composed of only physical sensor data ( $N_{ps} = 17$ ;  $N_{vs} = 0$ ) on the left side, and from the matrix composed of both physical sensors and their time histories ( $N_{ps} = 17$ ;  $N_{vs} = 17 \times 10$ ) on the right side. For the multi-time case, where 10 virtual sensors are considered for each physical sensor, a lobe pattern is identified, mostly at the end of the PSDF, as indicated with green dashed circles. Analysis of other cases show that this lobe pattern appears when more than one virtual sensor is used: the pattern depends on the sampling frequency and is independent of the number of physical sensors. To further investigate the root cause of appearance of this lobe pattern, two analytical cases are considered: (i) with one physical sensor and one time-delayed (virtual) sensor, and (ii) with one physical and two virtual sensors.

For the first case, let  $g(t)$  and  $h(t) = g(t + \Delta\tau)$  represent a physical sensor and its time-delayed signal, respectively ( $N_{ps} = N_{vs} = 1$ ).  $f(t) = g(t) + h(t)$ . The Fourier transform of  $f(t)$  reads

$$F(\omega) = G(\omega) + H(\omega), \tag{D1}$$

and

$$F^2 = FF^* = GG^* + GH^* + HG^* + HH^*, \tag{D2}$$

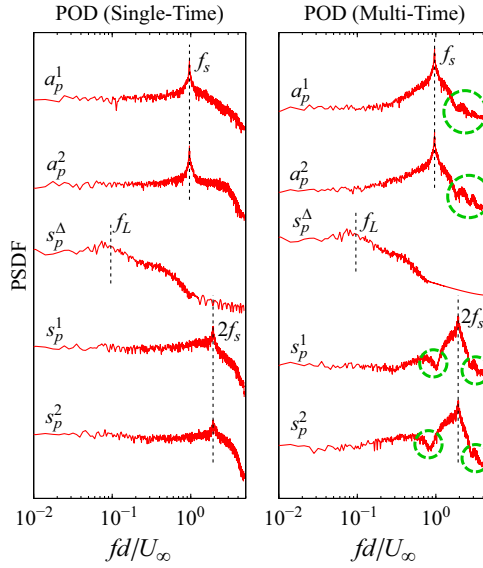


Figure 22. The PSDF of the temporal functions of the most energetic pressure POD modes. Left side obtained from the pressure matrix composed of only physical sensors ( $N_{ps} = 17$ ;  $N_{vs} = 0$ ) and right side from the pressure matrix composed of both physical and virtual sensors ( $N_{ps} = 17$ ;  $N_{vs} = 17 \times 10 = 170$ ). For a comparison with the SPOD multi-time pressure temporal coefficients, readers are referred to [figure 3](#).

where  $F^*$  is the conjugate function of  $F$  and the argument ( $\omega$ ) is implied for brevity. By definition

$$\begin{aligned}
 H(\omega) &= \int_{-\infty}^{\infty} h(t)e^{-i\omega t} dt \\
 &= \int_{-\infty}^{\infty} g(t + \Delta\tau)e^{-i\omega t} dt.
 \end{aligned}
 \tag{D3}$$

Now, let  $\xi = t + \Delta\tau$  and  $d\xi = dt$ . Then

$$H(\omega) = \int_{-\infty}^{\infty} g(\xi)e^{-i\omega(\xi-\Delta\tau)} d\xi = \int_{-\infty}^{\infty} g(\xi)e^{-i\omega\xi} d\xi e^{i\omega\Delta\tau} = G(\omega)e^{i\omega\Delta\tau}.
 \tag{D4}$$

Therefore

$$\begin{aligned}
 GH^* + HG^* &= GG^*e^{-i\omega\Delta\tau} + GG^*e^{i\omega\Delta\tau} \\
 &= 2GG^* \cos(\omega\Delta\tau),
 \end{aligned}
 \tag{D5}$$

and

$$HH^* = GG^*.
 \tag{D6}$$

Therefore,  $F^2$  can be expressed as

$$F^2 = 2GG^*(1 + \cos(\omega\Delta\tau)).
 \tag{D7}$$

The minimum of  $F^2$  happens at  $\omega_{min}\Delta\tau = \pi$  or  $\omega_{min} = \pi/\Delta\tau$ . As discussed in § 2.3,  $\Delta\tau = 1/10f_s$ . Therefore,  $\omega_{min} = 10\pi f_s = 5(2\pi f_s)$ , which is approximately 2.5 times larger than the Nyquist frequency related to the shedding frequency ( $\omega_{N(f_s)} = 2\pi(2f_s) = 2(2\pi f_s)$ ) and approximately 1.25 larger than the Nyquist frequency related to the second

harmonics ( $\omega_{N(2f_s)} = 2\pi(4f_s) = 4(2\pi f_s)$ ). Therefore, the frequency corresponding to the  $\omega_{min}$  will not be detected within the PSDF spectra in this case.

For the second case, let  $g(t)$  represent the physical sensor and  $h(t) = g(t + \Delta\tau)$  and  $k(t) = g(t + 2\Delta\tau)$  represent its two consecutive time-delayed signals ( $N_{ps} = 1$  and  $N_{vs} = 2$ ). Following the process outlined above

$$f(t) = g(t) + h(t) + k(t), \quad (D8)$$

$$F(\omega) = G(\omega) + H(\omega) + K(\omega), \quad (D9)$$

$$F^2 = GG^* + GH^* + GK^* + HG^* + HH^* + HK^* + KG^* + KH^* + KK^*. \quad (D10)$$

Similar to (D4)

$$K = G e^{2i\omega\Delta\tau}. \quad (D11)$$

Substituting (D11) and all other terms into (D10),  $F^2$  can be expressed as

$$\begin{aligned} F^2 &= 3GG^* + 4GG^* \cos(\omega\Delta\tau) + 2GG^* \cos(2\omega\Delta\tau) \\ &= GG^*(1 + 2\cos(\omega\Delta\tau))^2. \end{aligned} \quad (D12)$$

Here,  $F^2$  has a minimum at  $\omega_{min} = 2\pi/(3\Delta\tau) = 10(2\pi f_s)/3$ , which is less than  $\omega_{N(2f_s)}$ , and therefore will be detected in the PSDF of  $F^2$ .

Adding more virtual sensors further decreases  $\omega_{min}$  and results in observing more lobes within the spectra, as is the case on the right side of figure 22. It should be re-iterated that the lobe pattern is not observed with the SPOD modes, regardless of the number of virtual sensors or the sampling frequency, due to the convolution-filter operation.

#### REFERENCES

- ADRIAN, R.J. 1979 Conditional eddies in isotropic turbulence. *Phys. Fluids* **22** (11), 2065–2070.
- ADRIAN, R.J. & MOIN, P. 1988 Stochastic estimation of organized turbulent structure: homogeneous shear flow. *J. Fluid Mech.* **190**, 531–559.
- AMARAL, F.R., CAVALIERI, A.V.G., MARTINI, E., JORDAN, P. & TOWNE, A. 2021 Resolvent-based estimation of turbulent channel flow using wall measurements. *J. Fluid Mech.* **927**, A17.
- BENEDDINE, S., YEGAVIAN, R., SIPP, D. & LECLAIRE, B. 2017 Unsteady flow dynamics reconstruction from mean flow and point sensors: an experimental study. *J. Fluid Mech.* **824**, 174–201.
- BORÉE, J. 2003 Extended proper orthogonal decomposition: a tool to analyse correlated events in turbulent flows. *Exp. Fluids* **35** (2), 188–192.
- BOURGOIS, J.A., NOACK, B.R. & MARTINUZZI, R.J. 2013 Generalized phase average with applications to sensor-based flow estimation of the wall-mounted square cylinder wake. *J. Fluid Mech.* **736**, 316–350.
- BOURGOIS, J.A., SATTARI, P. & MARTINUZZI, R.J. 2011 Alternating half-loop shedding in the turbulent wake of a finite surface-mounted square cylinder with a thin boundary layer. *Phys. Fluids* **23** (9), 095101.
- CHEN, Z., LIN, Z., ZHAI, X. & LIU, J. 2022 Dynamic wind turbine wake reconstruction: a Koopman-linear flow estimator. *Energy* **238**, 121723.
- CUÉLLAR, A., GÜEMES, A., IANIRO, A., FLORES, Ó., VINUESA, R. & DISCETTI, S. 2024 Three-dimensional generative adversarial networks for turbulent flow estimation from wall measurements. *J. Fluid Mech.* **991**, A1.
- DENG, ZH, CHEN, Y., LIU, Y. & KIM, K.C. 2019 Time-resolved turbulent velocity field reconstruction using a long short-term memory (LSTM)-based artificial intelligence framework. *Phys. Fluids* **31** (7), 075108.
- DISCETTI, S., BELLANI, G., ÖRLÜ, R., SERPIERI, J., SANMIGUEL VILA, C., RAIOLA, M., ZHENG, X., MASCOTELLI, L., TALAMELLI, A. & IANIRO, A. 2019 Characterization of very-large-scale motions in high-Re pipe flows. *Exp. Therm. Fluid Sci.* **104**, 1–8.
- DISCETTI, S., RAIOLA, M. & IANIRO, A. 2018 Estimation of time-resolved turbulent fields through correlation of non-time-resolved field measurements and time-resolved point measurements. *Exp. Therm. Fluid Sci.* **93**, 119–130.
- DURSAISAMY, K., IACCARINO, G. & XIAO, H. 2019 Turbulence modeling in the age of data. *Annu. Rev. Fluid Mech.* **51** (1), 357–377.

- DURGESH, V. & NAUGHTON, J.W. 2010 Multi-time-delay LSE-POD complementary approach applied to unsteady high-Reynolds-number near wake flow. *Exp. Fluids* **49** (3), 571–583.
- GOMEZ, D.F., KIRK, P.B., LIND, A.H., JONES, A.R., PALEY, D.A. & LAGOR, F.D. 2019 Unsteady DMD-based flowfield estimation from embedded pressure sensors in an actuated airfoil. In *AIAA Scitech 2019 Forum, Paper: AIAA 2019-0346*.
- HOLMES, P., LUMLEY, J.L., BERKOOZ, G. & ROWLEY, C.W. 2012 *Turbulence, Coherent Structures, Dynamical Systems and Symmetry*. Cambridge University Press.
- HOSSEINI, Z., BOURGEOIS, J.A. & MARTINUZZI, R.J. 2013 Large-scale structures in dipole and quadrupole wakes of a wall-mounted finite rectangular cylinder. *Exp. Fluids* **54** (9), 1595.
- HOSSEINI, Z., MARTINUZZI, R.J. & NOACK, B.R. 2015 Sensor-based estimation of the velocity in the wake of a low-aspect-ratio pyramid. *Exp. Fluids* **56** (1), 13.
- HOSSEINI, Z., MARTINUZZI, R.J. & NOACK, B.R. 2016 Modal energy flow analysis of a highly modulated wake behind a wall-mounted pyramid. *J. Fluid Mech.* **798**, 717–750.
- HUNT, J.C.R., ABELL, C.J., PETERKA, J.A. & WOO, H. 1978 Kinematical studies of the flows around free or surface-mounted obstacles; applying topology to flow visualization. *J. Fluid Mech.* **86** (1), 179–200.
- HUSSAIN, A.K.M.F. 1983 Coherent structures - reality and myth. *Phys. Fluids* **26** (10), 2816–2850.
- HUSSAIN, A.K.M.F. & REYNOLDS, W.C. 1970 The mechanics of an organized wave in turbulent shear flow. *J. Fluid Mech.* **41** (2), 241–258.
- JIN, X., LAIMA, S., CHEN, W.L. & LI, H. 2020 Time-resolved reconstruction of flow field around a circular cylinder by recurrent neural networks based on non-time-resolved particle image velocimetry measurements. *Exp. Fluids* **61** (4), 114.
- KINDREE, M.G., SHAHROODI, M. & MARTINUZZI, R.J. 2018 Low-frequency dynamics in the turbulent wake of cantilevered square and circular cylinders protruding a thin laminar boundary layer. *Exp. Fluids* **59** (12), 186.
- KUTZ, J.N. 2017 Deep learning in fluid dynamics. *J. Fluid Mech.* **814**, 1–4.
- MANOHAR, K.H., MORTON, C. & ZIADÉ, P. 2022 Sparse sensor-based cylinder flow estimation using artificial neural networks. *Phys. Rev. Fluids* **7** (2), 024707.
- MARTINI, E., CAVALIERI, A.V.G., JORDAN, P., TOWNE, A. & LESSHAFFT, L. 2020 Resolvent-based optimal estimation of transitional and turbulent flows. *J. Fluid Mech.* **900**, A2.
- MOHAMMADI, A., MORTON, C. & MARTINUZZI, R.J. 2022 Effect of boundary layer state on the wake of a cantilevered square cylinder of aspect ratio 4. *Phys. Rev. Fluids* **7** (8), 84702.
- MOHAMMADI, A., MORTON, C. & MARTINUZZI, R.J. 2023 Benefits of FIR-based spectral proper orthogonal decomposition in separation of flow dynamics in the wake of a cantilevered square cylinder. *Intl J. Heat Fluid Flow* **104** (December), 109224.
- NOACK, B.R. 2006 *Niederdimensionale Galerkin-Modelle Fur Laminare Und Transitionelle Freie Scherströmungen*. Habilitationsschrift, Technische Universität Aachen.
- NOACK, B.R., AFANASIEV, K., MORZYNSKI, M., TADMOR, G. & THIELE, F. 2003 A hierarchy of low-dimensional models for the transient and post-transient cylinder wake. *J. Fluid Mech.* **497**, 335–363.
- NOACK, B.R., PAPAS, P. & MONKEWITZ, P.A. 2005 The need for a pressure-term representation in empirical Galerkin models of incompressible shear flows. *J. Fluid Mech.* **523**, 339–365.
- ROWLEY, C.W., MEZIC, I., BAGHERI, S., SCHLATTER, P. & HENNINGSON, D.S. 2009 Spectral analysis of nonlinear flows. *J. Fluid Mech.* **641**, 115–127.
- SAKAMOTO, H. & ARIE, M. 1983 Vortex shedding from a rectangular prism and a circular cylinder placed vertically in a turbulent boundary layer. *J. Fluid Mech.* **126**, 147–165.
- SAKAMOTO, H. & OIWAKE, S. 1984 Fluctuating forces on a rectangular prism and a circular cylinder placed vertically in a turbulent boundary layer. *J. Fluids Engng* **106** (June), 160–166.
- SASAKI, K., PIANTANIDA, S., CAVALIERI, A.V.G. & JORDAN, P. 2017 Real-time modelling of wavepackets in turbulent jets. *J. Fluid Mech.* **821**, 458–481.
- SCHMID, P.J. 2010 Dynamic mode decomposition of numerical and experimental data. *J. Fluid Mech.* **656**, 5–28.
- SICOT, C., PERRIN, R., TRAN, T.T. & BORÉE, J. 2012 Wall pressure and conditional flow structures downstream of a reattaching flow region. *Intl J. Heat Fluid Flow* **35**, 119–129.
- SIEBER, M., PASCHEREIT, C.O. & OBERLEITHNER, K. 2016 Spectral proper orthogonal decomposition. *J. Fluid Mech.* **792**, 798–828.
- SIROVICH, L. 1987 Turbulence and the dynamics of coherent structures. I. Coherent structures. *Q. Appl. Math.* **45** (3), 561–571.
- TAYLOR, J.A. & GLAUSER, M.N. 2004 Towards practical flow sensing and control via POD and LSE based low-dimensional tools. *Trans. ASME J. Fluids Engng* **126** (3), 337–345.

- TOWNE, A., LOZANO-DURAN, A. & YANG, X. 2020 Resolvent-based estimation of space-time flow statistics. *J. Fluid Mech.* **883**, A17.
- TU, J.H., GRIFFIN, J., HART, A., ROWLEY, C.W., CATTAFESTA, L.N. & UKEILEY, L.S. 2013 Integration of non-time-resolved PIV and time-resolved velocity point sensors for dynamic estimation of velocity fields. *Exp. Fluids* **54** (2), 1429.
- WANG, H.F., ZHOU, Y., CHAN, C.K. & LAM, K.S. 2006 Effect of initial conditions on interaction between a boundary layer and a wall-mounted finite-length-cylinder wake. *Phys. Fluids* **18** (6), 065106.
- WIENEKE, B. 2015 PIV uncertainty quantification from correlation statistics. *Meas. Sci. Technol.* **26** (7), 074002.